The Aerodynamic Design and Evaluation of a Low Specific Speed Turbo Compressor

Andrew Vine

Imperial College London
Department of Mechanical Engineering

Submitted for the degree of Doctor of Philosophy of the University of London
and the Diploma of Imperial College.
September 2005

Abstract

A compressor with a low shaft speed, high pressure rise and low flow rate has a low specific speed. Such compressors are needed for low flow rate applications when the shaft speed is fixed by the constraints of other machinery, or by cost. Low specific speed turbo-compressors are inefficient because parasitic losses represent a greater proportion of the work at low flow rates. The energy lost to surface friction on the back face of the compressor rotor (windage), or the leakage between stages are examples of parasitic losses. Therefore positive displacement machines are often used for low specific speed applications despite problems of high cost and complexity, the requirement for high maintenance, large size and weight, and oil ingestion.

Turbo compressors do not suffer from these problems, therefore the objective of this research is to extend the range of turbo-compressors to operate at lower specific speeds. The requirement to minimise windage, forces a reduction in rotor tip speed, and the requirement for a high pressure ratio gives rise to a design with highly forward swept rotor blades. The resistance to surge of this design is discussed.

This design was evaluated experimentally and the best performance was obtained at a referred shaft speed of 20,000rpm at a pressure ratio of 1.52, a referred flow rate of 77g/s and an efficiency of 49% ± 3.1 percentage points.

The design was also assessed using the CFD package CFX Tascflow. Grid independence could not be established due to constraints of computer resources and problems with this specific design. Examination of the results suggests that a transient sliding mesh interface may be required between the rotor and stator, rather than the frozen rotor interface that was used.

Designs based on this concept could provide a benefit if used in the later stages of a multistage industrial compressor as the compressor that was tested has a similar specific speed and efficiency to existing designs, and a substantially greater pressure ratio.

Acknowledgements

I would like to thank my supervisors Keith Pullen and Shahram Etemad for allowing me the freedom to pursue and develop my ideas. I would also like to thank Niall McGlashan for all his technical help and advice. Thanks also to Warren Thornton for listening to my ideas and working with me on this project. Finally my thanks go to all the friends I have known at Imperial College.

Nomenclature

Symbol	Meaning
a	Radius of windage face
A	Flow cross sectional area
b	Blade height
C	Absolute gas velocity
C_p	Specific heat at constant pressure
D	Diameter
h	Specific enthalpy
H_d	Dynamic head
H	Heat
I	Current
k	Turbulent kinetic energy / constant
K	Windage coefficient (C_m in Daily's work)
N	Rotational Speed (RPM)
N_s	Specific speed
P	Pressure
Q	Volumetric flow
R	Resistance / Gas constant
Re	Reynolds number
s	Axial windage gap
S_x	X generated due to sources
T	Temperature / Turbulent intensity
U	Speed
u^+	Near wall dimensionless velocity
v	Specific volume
W	Gas velocity relative to rotor / Work
y^+	Dimensionless distance from the wall
μ	Viscosity
ρ	Density
Π_3	Power co-efficienct
ω	Angular velocity
τ	Torque / Shear stress
ΔX	Change / error in X
$\dot{X}$	Rate of change of X
γ	Ratio of specific heats
ϕ	Flow co-efficient dummy quantity
ψ	Head co-efficient
Φ	Internal Energy generated by viscous shear
ν	Kinematic viscosity ($\nu = \frac{\mu}{\rho}$)
Γ	Diffusivity
κ	Von Karman's Constant

Subscripts

Symbol	Meaning
$1, 2, 3$	Station numbers
0	Total conditions
inf	At infinity
m	Meridional
opt	Optimum
p	Polytropic
r	Radial component
ref	Reference condition
s	Isentropic
w	Windage
θ	Tangential component

Contents

1 Introduction

This research began in response to the problem of compressing fuel gas for micro gas turbine generation sets. It was proposed that gen-sets of approximately 100kW could be used to generate electricity for small scale and domestic use. The gen-sets would be small, cheap, clean, and quiet and therefore they could be sited near to the point of use, enabling the use of the high grade waste heat for domestic heating [1]. If natural gas were used as the fuel then it would require compression to the compressor exit pressure so that it could pass into the combustion chamber. Pilot schemes showed that the compression of gas was a major problem. Gas compressors were typically larger than the gen-set itself and there were problems with reliability.

Turbo-compressors consist of rotating bladed assemblies which accelerate the gas and then diffuse it to recover kinetic energy as pressure. Turbo-compressors are efficient and reliable, but are still not suitable for every application as they do not work well at low flow rates and shaft speeds. Positive displacement machines work by enclosing a fixed volume of gas, reducing its volume and then exhausting it, and they are favoured at low flow rates despite problems of large size and weight, high cost and the requirement of frequent maintenance.

It would be preferable to use turbo-machinery for fuel gas compression as it is generally more reliable, efficient and compact. However this is not straightforward as the gas flow rate is very low (approximately $10gs^{-1}$). This statement can be expressed more elegantly with a consideration of dimensionless specific speed which is discussed later in this section.

The objective of the research was originally to build a turbo-compressor that could work efficiently at the low flow rates required. An efficient compressor of this type could replace positive displacement machines in many applications, although this objective is highly ambitions. In researching the field of low flow rate turbo-machinery, it was discovered that compressors of a similar specification were used in the final stages of multiple stage radial compressors. This provided a useful starting point for the research.

In this section, a dimensional analysis of a generic gas or air compressor is discussed. This analysis can be used when scaling a known compressor to other sizes, and also leads to the definition of specific speed. The need for low specific speed compressors is discussed.

The field of low specific speed turbo-compressors is explored in detail. The performance of positive displacement compressors is of interest, but there is little common design methodology so they are mentioned only briefly. The conventional approach to designing low specific speed turbo-compressors is discussed, including how their performance is measured and why they are not very efficient. Finally some unconventional designs are discussed and their performance is compared.

1.1 Turbo-compressor Dimensional Analysis

This discussion of dimensionless groups is largely taken from Japikse and Baines[2] and its reference Shepard[3]. A dimensional analysis of a generic compressor yields five dimensionless groups. Some texts use slightly different versions of the dimensionless groups as a result of choices made at an early stage of the analysis. The alternatives are shown as dashed quantities. The station number subscripts refer to **Figure 1** and U refers to the blade speed.

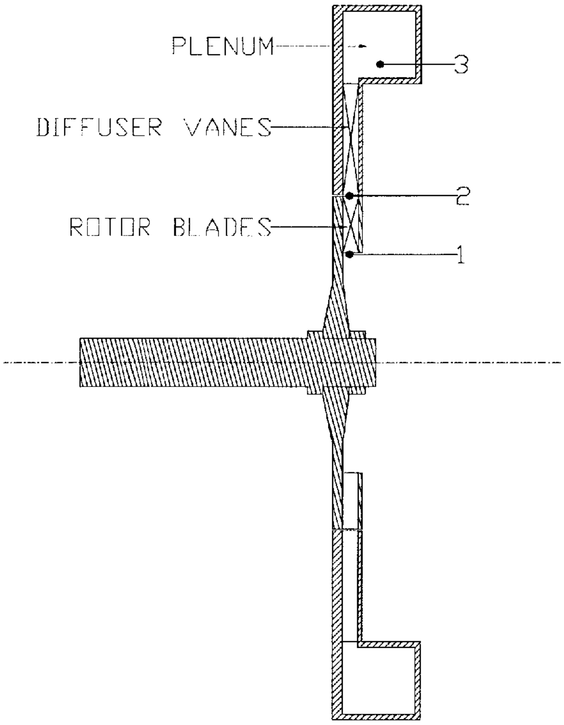

Figure 1: Station numbers

Flow coefficient

$$\phi = \frac{\dot{Q}_1}{U_2 D^2} \tag{1}$$

Head coefficient

$$\psi = \frac{\Delta h_{0s}}{U_2^2} \tag{2}$$

$$\psi' = \frac{gH_d}{U_2^2} \tag{3}$$

Power coefficient

$$\Pi_3 = \frac{\Delta h_0}{h_{01}} \tag{4}$$

Rotational Reynolds number

$$Re = \frac{\rho U_2 D_2}{\mu} \tag{5}$$

$$Re' = \frac{\rho U_2 b_2}{\mu} \tag{6}$$

Blade Mach number (Velocity ratio)

$$M_u = \frac{U_2}{a_{01}} = \frac{ND_2}{a_{01}} \tag{7}$$

1.1.1 Turbo-compressor Scaling

The essential turbomachinery parameters can be derived from these dimensionless groups. These parameters provide a means of comparing compressors that perform a wide variety of duties. The five parameters have many uses, one of which is scaling. Scaling is used when an existing compressor design is adapted for a different application. The following discussion deals with the prediction of the change in performance due to a simple change in size, but it is also possible to predict the change in performance for different gas properties. If all the parameters which affect performance have been considered in the dimensionless analysis, and all the dimensionless groups remain the same throughout the scaling, then the flow and therefore the performance of the new machine will be identical [4].

The velocity ratio (Equation 7) shows that the blade speed (U_2) must be kept constant by scaling the rotational speed by the reciprocal of the geometric scale factor. Having fixed the blade speed, the flow coefficient can be kept constant by keeping the same meridional speed at entry (in this case the meridional speed is the gas radial speed). This means that the mass flow rate will be scaled by the square of the geometric scaling factor. With these two parameters fixed the head and power coefficients follow. This leaves the Reynolds number, which cannot be scaled properly without adjusting the gas properties. The Reynolds number can be thought of as the ratio of inertial forces to vicious forces. It is important in predicting laminar to turbulent transitions and wall friction losses. Wall friction losses have a greater effect on efficiency at smaller sizes, but they are generally not the dominant loss mechanism in turbomachinery; the lack of similarity is often ignored. However, the change in efficiency due to the change in Reynolds number can be calculated by semi-empirical methods such as Casey[5].

1.2 Efficiency

1.2.1 Isentropic Efficiency

The efficiency of a compressor is an important performance parameter. In the following chapters, "efficiency" refers to the isentropic, adiabatic efficiency, unless otherwise stated. This is a comparison between the work input for the actual compressor and the work input for an ideal adiabatic compressor with the same inlet conditions and pressure ratio.

1.2.2 Polytropic Efficiency

When comparing compressor stages of different pressure ratios, the isentropic efficiency cannot be used; the correct parameter is the polytropic efficiency. If two compressors with an efficiency of 80% and a pressure ratio of 2 : 1 are arranged in series, then the overall efficiency will be less than 80%. This is because in the second compressor the work input is compared to an isentropic compressor with a higher inlet temperature than the first and greater amount of work is required to compress hotter gas. Therefore a single stage compressor with a pressure ratio of 4 and an efficiency of 80% is aerodynamically superior to either of the 2:1 stages mentioned above. The polytropic efficiency allows a fair comparison of compressors of different pressure ratios. It can be calculated using Equation 8.

$$\eta_p = \frac{\gamma - 1}{\gamma} \frac{\ln \frac{P_3}{P_1}}{\ln \frac{T_3}{T_1}} \tag{8}$$

Figure 2 shows the relationship between isentropic efficiency, polytropic efficiency and pressure ratio. It shows that a 4:1 compressor of $\eta_s = 78\%$ has the same polytropic efficiency as a 2:1 compressor of $\eta_s = 80\%$. A compressor made from stages of identical polytropic efficiency will have the same overall polytropic efficiency.

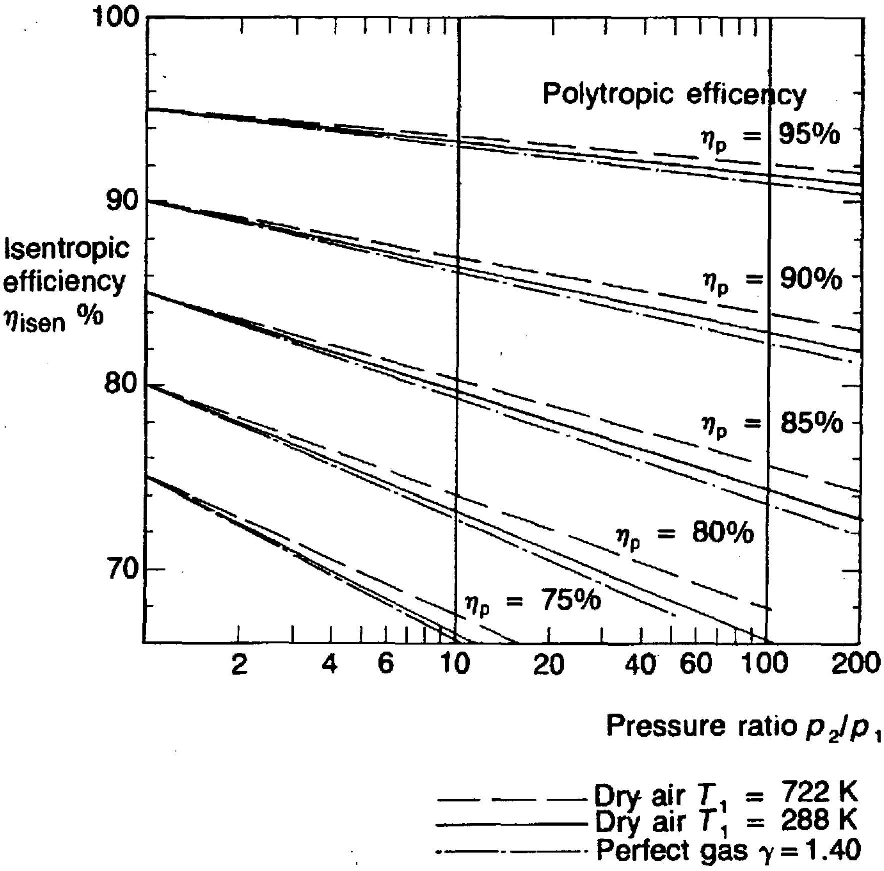

Figure 2: Isentropic Efficiency vs Pressure Ratio[6]

1.2.3 Isothermal Efficiency

The isentropic efficiency considers a compressor that is perfectly insulated as the ideal compressor, whereas the isothermal efficiency considers a reference compressor that is perfectly cooled, such that the gas temperature does not change during compression.

The work done by a reversible compressor is given by **Equation 9**

$$w_{rev} = \int_{in}^{out} v dP \tag{9}$$

The work is minimised when the specific volume is minimised throughout the process, and this can be achieved by cooling. Therefore the ideal work for an isothermal compression is less than the ideal work for an isentropic, adiabatic compression. Indeed, for a well cooled compressor the actual work may be less than the ideal adiabatic work. This would lead to an efficiency greater than 100% and therefore in the case of well cooled compressors the isothermal efficiency should be used. If the objective is to minimise the work input to achieve a given pressure then the compressor should be cooled.

1.3 Specific Speed - Origin, Definition and Significance

Non-dimensional Specific speed is calculated by combining the flow co-efficient and the head coefficient.

$$N_s \propto \phi^{\frac{1}{2}} / \psi^{\frac{3}{4}} \tag{10}$$

The flow coefficient is a measure of how fast fluid is passing through the machine relative to the rotor tip speed. The head coefficient is a ratio of the pressure rise and the square of the blade speed. A machine of a given rotational speed with a high pressure rise and a low volumetric flow and low shaft speed has a low specific speed. Specific speed can be re-arranged to:

$$N_s = \frac{\omega \dot{Q}^{\frac{1}{2}}}{\Delta h^{\frac{3}{4}}} \tag{11}$$

or

$$N_s' = \frac{\omega \dot{Q}^{\frac{1}{2}}}{(gH_d)^{\frac{3}{4}}} \tag{12}$$

Specific speed is used in design to choose the type of machine that is suitable for an application and to find the best shaft speed for the design point pressure rise and volumetric flow rate. Many texts show the graph in **Figure 3**. The most efficient machines to date are plotted on a graph of specific speed versus efficiency. Although machine performance has improved since 1990 when this version of the graph was first published, the same trends are observed. For each type of machine there is an optimum specific speed.

1.4 The Necessity of Low Specific Speed Compression

As **Figure 3** shows, axial turbo-compressors are the most efficient means of compressing gas currently known. However, for small machines it is not always possible to achieve the performance that **Figure 3** implies. **Figure 4** recasts the data from **Figure 3** for the compression of air from atmospheric pressure to a pressure ratio of 3. If the specific speed is held constant as the machine is scaled down, the speed of the machine increases. Calculations show that to compress $10gs^{-1}$ of air at a pressure ratio

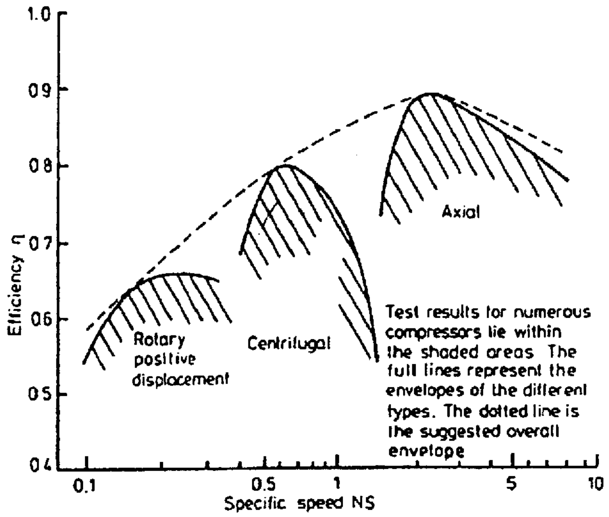

Test results for numerous compressors lie within the shaded areas. The full lines represent the envelopes of the different types. The dotted line is the suggested overall envelope

Figure 3: Specific Speed vs Efficiency[7]

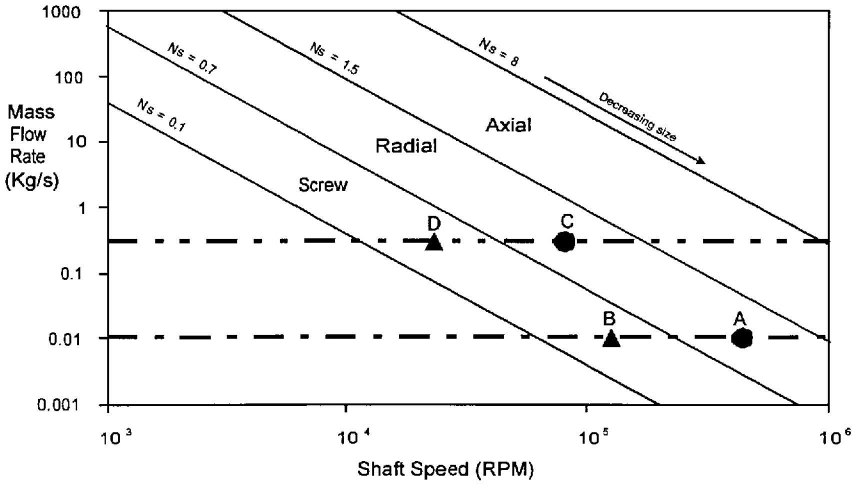

Figure 4: Speed and mass flow range of air compressor types at PR=3

of 3, a rotor of 18mm diameter would be required to run at 500,000rpm for a radial compressor (represented by point A on **Figure 4**). This shaft speed is not feasible for reasons discussed later. An axial compressor would be smaller and faster still. This is similar to the gas turbine fuel application and explains why positive displacement machines are used exclusively. Indeed the screw compressor (point B) also requires a relatively high shaft speed of 130,000rpm and therefore lower specific speed compressors, such as sliding vane or scroll compressors, are generally favoured for very low flow rates.

At these very small sizes the efficiency of turbomachines is reduced due to greater wall friction losses. This is a well-known phenomenon and semi-empirical methods based on the Reynolds number can be used to predict the efficiency penalty for scaling a turbo-machine down, such as the methods described by Casey [5]. An initial study using Casey's method shows that a compressor for $300gs^{-1}$ with a 95mm rotor diameter scaled down to $10gs^{-1}$ would suffer a drop in efficiency of 11% from 80% to 69%. However, in a compressor using tolerances scaled down by the same factor, cost would not scale with size and the smaller compressor would be less economically attractive. For this reason, small compressors rarely achieve the efficiency that would be predicted simply by taking additional Reynolds losses into account, because clearances are relatively larger (due to larger relative tolerances).

The smallest compressors in common use are found in automotive turbochargers, where the necessity of cheap manufacture causes large relative tip clearances and the resulting efficiency penalty [4]. Turbochargers can also be made cheaply because there is a high pressure oil system available allowing the use of cheap hydrodynamic bearings. The low stiffness of such bearings mean that tip clearance is further compromised.

Even at a size where efficient turbo-machinery is feasible (approximately 300g/s, represented by point C), there is still a significant problem providing shaft power at high speed and at a reasonable cost. Low speed motors with gearboxes are large and require high maintenance, and until recently a high-speed electric motor of sufficient power has been too expensive. Positive displacement machines (point D) dominate this market because they can take advantage of low speed motors, although recently, turbo-compressors that are directly driven from a high speed motor have entered the market [8].

The final situation that would necessitate low specific speed compression is when the shaft speed is chosen by other considerations than the needs of the stage. This occurs commonly in multiple stage industrial compressors where the volumetric flow rate reduces as the gas is compressed, and therefore the later stages have a lower specific speed. Low specific speed stages are particularly favoured because they have no inducer and therefore have a low axial length, so that the rotating assembly can remain short and stiff (discussed further in Section 1.6.6). High diameter rotors are generally avoided when the specific speed of the stage is low because this would lead to excessively low flow coefficients causing high wall friction, and therefore the rotors are generally light. This is desirable as adding mass to the shaft would reduce its natural frequency. They also run at low speed and thus avoid high excitation frequencies that are likely to coincide with shaft modes.

1.5 Positive Displacement Compressors

Typically a positive displacement machine will be chosen for low specific speed applications. These machines work by enclosing a fixed volume of gas, reducing its volume by a compression ratio that is fixed by the machine's geometry, and then exhausting the gas. The following discussion of positive displacement compressors is taken from Vine et al [9]. The most common types of positive displacement compressors are shown in **Figure 5**.

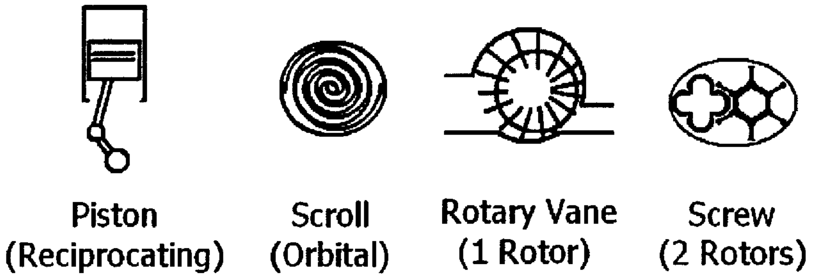

Figure 5: Common types of positive displacement compressor [9]

Reciprocating Compressors are the largest and slowest of positive displacement machines. They operate efficiently, although they require frequent maintenance. Oil ingesting designs require filtration and oil-free designs have a limited pressure ratio due to the temperature limits of the piston rings.

Scroll Compressors are used for very low mass flow rates and operate without oil flooding. There is one product on the market for fuelling micro turbines [10], as they are a relatively new technology. They have a limited service life and their reliability is not established.

Rotary Vane compressors typically ingest oil, which requires the usual removal process. They are reasonably reliable, cheap to manufacture, and require minimal maintenance. Their size is moderate when compared to other positive displacement machines.

Screw Compressors work at the higher end of the specific speed range for positive displacement machines, requiring much higher shaft speeds. They are more reliable and compact than other positive displacement machines and operate with reasonable efficiently. Oil ingesting designs require filtration. Oil-free designs require precision

Table 1: Commercially Available Positive Displacement Compressors [9]

	Power (kW)	Massflow (g/s)	PR	η_s %	Size (mm)	Weight (kg)	Power density (W/kg)
Reciprocating - Air	3.7	10.6	5.4	51	1200 x 1700 x 600	286	12.9
	15	49.7	5.4	60	1900 x 2000 x 1100	818	18.3
Screw - Air	7.4	22	8.5	72	680 x 680 x 860	159	46.5
	22	68.5	8.5	74	860 x 860 x 1320	359	61.3
Rotary Vane Gas	4	6.6	6	52	-	155	25.8
	5.5	10	6	57	-	155	35.5
	7.5	14	6	59	-	155	48.4
	18.5	32	6	55	-	428	43.2
Scroll Gas	6	8.84	5.78	48	1070 x 610 x 1370	250	24

timing gears and very high manufacturing tolerances for a complex geometry.

Table 1 shows quantitative data for the comparison of positive displacement compressors. Screw compressors have the highest power density of the positive displacement machines. In summary, positive displacement machines have the disadvantages of large size and weight, high complexity, the requirement for frequent maintenance, oil ingestion, and high cost.

1.6 Conventional Low Specific Speed Turbo-compressor Design Considerations

In the following section, the problems of designing low specific speed radial stages, and the normal methods of alleviating these problems are discussed.

Specific speed is a misleading name; shape factor would be more appropriate as Whitfield and Baines [7] suggest. **Figure 6** shows three rotors of different specific speeds. The low specific speed rotor has a large diameter since enthalpy rise increases with diameter. It has a low exit blade height because of the low volumetric flow rate.

Figure 3 shows that the efficiency of a compressor decreases at a specific speed below the optimum, this phenomenon is explained in the following section.

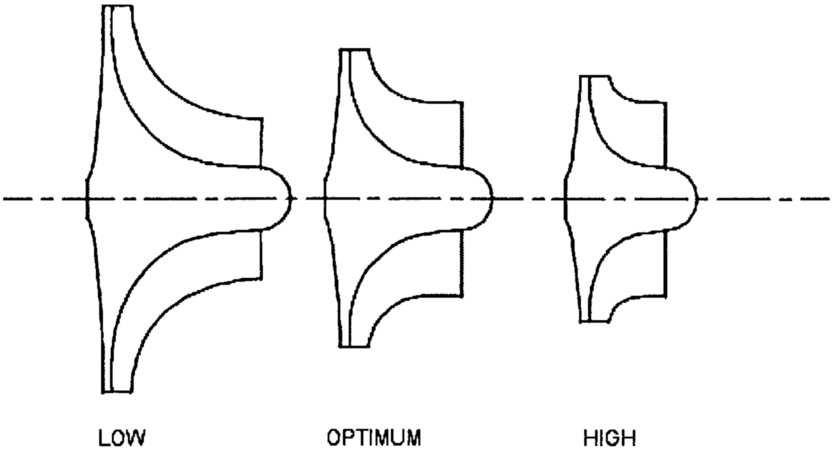

Figure 6: Rotors of low, optimum, and high specific speed

1.6.1 Parasitic Losses

Consider two compressors, one of optimum specific speed, and a second with the same diameter, shaft speed and blade angles but a lower blade height and therefore a lower specific speed. The major losses in a well designed compressor come from mixing losses at the rotor exit, windage (power absorbed by wall friction on the compressor back face), blade tip leakage, shaft seal leakage, and passage wall friction. The windage and leakage will remain very similar in the cropped blade compressor, but will carry a greater efficiency penalty because the mass flow rate and therefore the work input of the cropped blade compressor is lower. The pipe loss associated with the flow passing down the rotor and stator passages also represents a greater efficiency penalty for the cropped blade compressor because it has more wall area per unit mass flow than the un-cropped compressor (although strictly this is not a parasitic loss).

1.6.2 Optimization of Number of Stages for Low Specific Speed Compressor

Consider the case of a multi-stage compressor of a fixed pressure ratio, shaft speed and low flow rate where the number of stages must be chosen. The definition of specific speed (**Equation 11**) reveals that choosing a greater number of stages will increase the specific speed of each stage by decreasing the enthalpy rise per stage, allowing more efficient compression. However, too many stages will cause the shaft to be too long causing rotor dynamics problems and the extra complexity caused by many stages will also increase the cost. Therefore there is an optimum number of stages for a given specification.

For a given shaft speed, work input to the gas varies with the square of diameter whereas windage varies with the 4.5th power (see Section 2.1.1). It is entirely possible that windage can become the dominant loss mechanism, unless the tip speed is limited. This explains why pressure ratios are generally low for low specific speed stages. Casey et al [11] quote typical tip Mach numbers of 0.4-0.7 and pressure ratios between $1.2-1.6$ for compressors for the condition $0.004 > \phi > 0.0018$ and down to a specific speed of 0.25. Conventional radial compressors of higher flow coefficient typically have tip Mach numbers well in excess of Mach 1. See Section 2.1.1 for a more detailed discussion of windage.

1.6.3 Rotor Shroud

Since tip leakage is a serious concern, low specific speed impellers are normally shrouded as shown in **Figure 7**. Shrouded impellers have a lower maximum tip speed (shrouded:

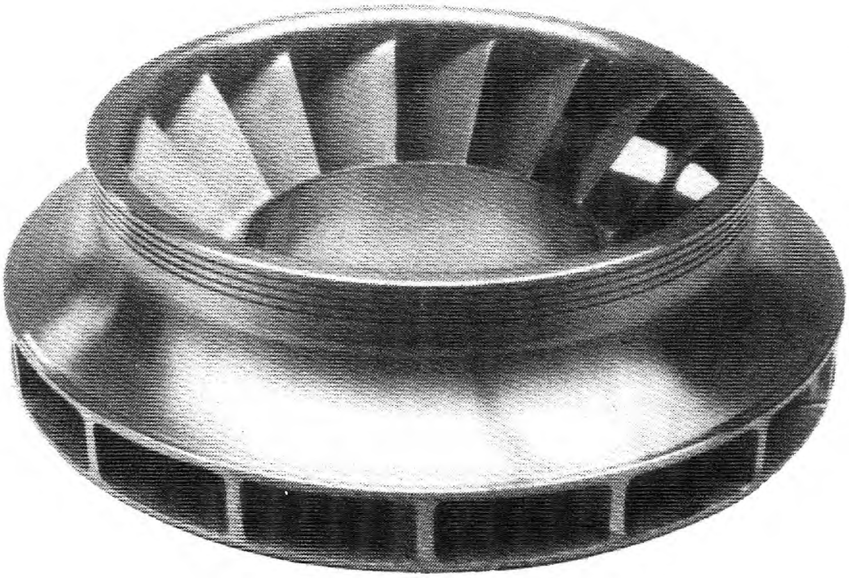

Figure 7: Rotor with shroud [6]

$300ms^{-1} - 360ms^{-1}$ unshrouded: $380ms^{-1} - 430ms^{-1}$, Cumpsty [6]) due to stress considerations, but in low specific speed stages, the tip speed is already low to minimise windage (about $200ms^{-1}$).

1.6.4 Optimisation of Backsweep

Casey et al [11] show that if backsweep is increased then there are two competing effects on the pipe losses. Firstly the flow path length is increased leading to greater loss. Secondly the width between the blades in the r-θ plane is decreased allowing an increase in blade height. This causes an increase in the effective hydraulic diameter, and a reduction in wall friction losses. Casey et al [11] report that in some cases increased backsweep can cause an increase in pressure ratio because the reduction in

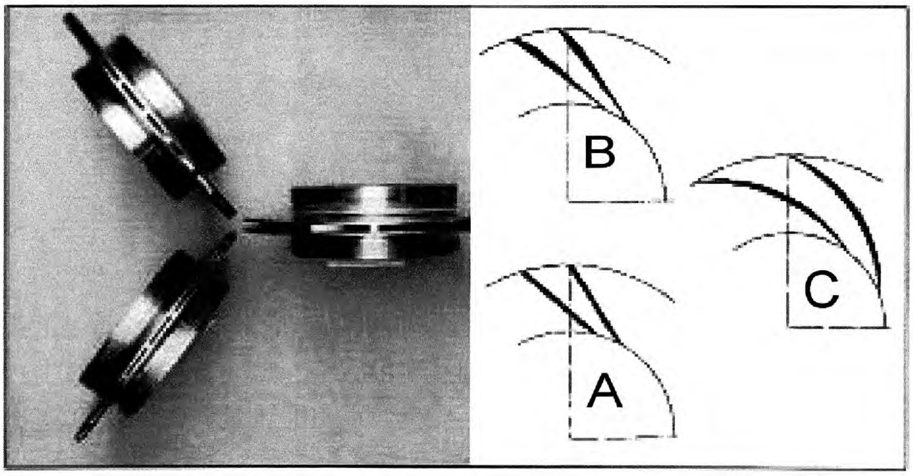

Figure 8: Photographs of rotors A, B, and C showing low blade heights (Left) and corresponding blade profile (right) [12]

pipe loss outweighs the reduction in momentum transferred to the fluid, and goes on to find the optimum backsweep. (**Figure 8**) shows three rotors A, B, and C, increasing in backsweep from A to C. Of these, C had the highest efficiency, although efficiency decreased if the backsweep was increased further.

1.6.5 High Diffuser Inlet Flow Angle

In a low specific speed stage the rotor must be of a reasonable diameter in order to produce a pressure rise, and the volumetric flow rate must be low. This means that the rotor must be large relative to the volumetric flow rate, which means that the radial velocity must be low (an alternative view is that if $N_s \propto \phi^{\frac{1}{2}}/\psi^{\frac{3}{4}}$ then the flow coefficient must be small for low specific speed as the head coefficient is limited by tip speed). The tangential component of velocity at rotor exit must be high in order to transfer momentum to the fluid. Therefore a low specific speed compressor will have a high rotor exit flow angle. Many introductory texts on the design of radial compressors warn of problems associated with high flow angles. Watson and Janota [13] quote the parameter $\lambda = C_\theta / C_r$ and warns of potential problems in a vaneless diffuser or space should this value exceed 4 - equivalent to 75 degrees to the radial direction.

The problem with high diffuser inlet angles is that the vaneless space is prone to stalling as described by Jansen [14]. The flow in the vaneless space is similar to a free vortex; the pressure increases in the radial direction. This means that all the fluid in the diffuser experiences a force towards the axis of the machine. **Figure 9** shows a normal vaneless diffuser where the back pressure is too high. The flow at a plane mid-way between the diffuser walls takes the path between A and B. However the flow in the boundary layer is slower (represented by the smaller vectors). Therefore the pressure gradient has a greater effect because the flow has less momentum and therefore the flow path is more curved. Jansen [14] assumes that when the boundary flow reaches the tangential direction (point C) the flow reverses and the diffuser stalls. **Figure 10** shows that the problem is more severe in diffusers with a high inlet angle. The flow has to deviate less in order to reach the tangential direction and therefore the stall begins at a lower radius (point D).

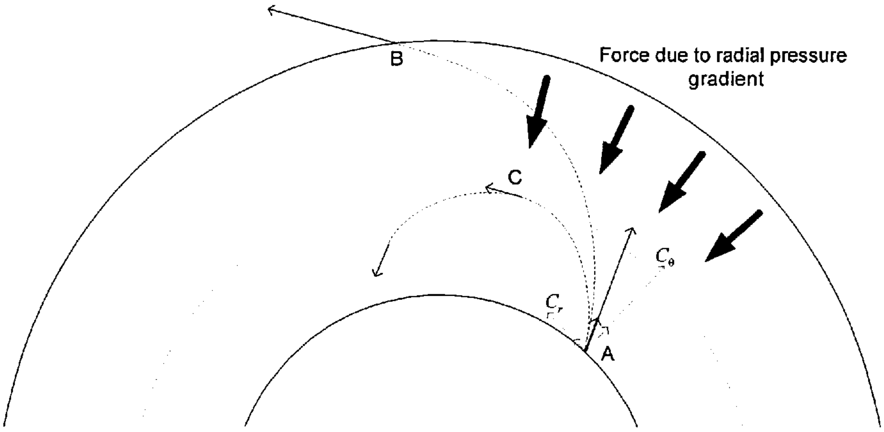

Figure 9: Boundary layer back-flow in a vaneless diffuser

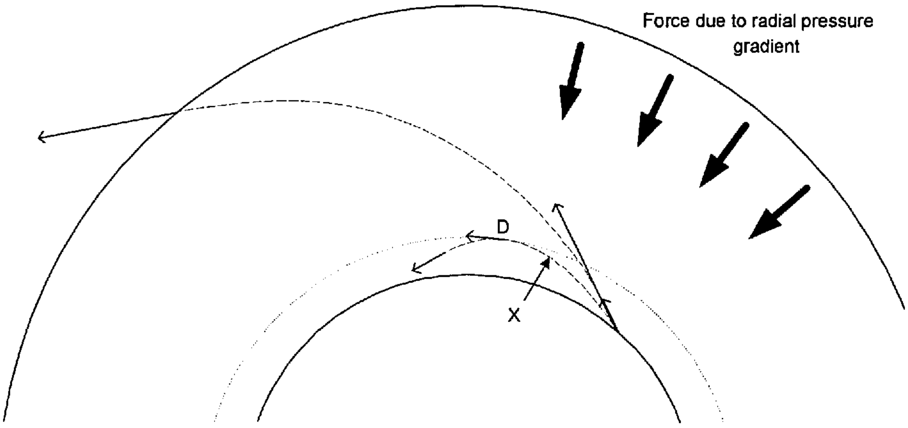

Figure 10: Early back flow in the boundary layer caused by increased diffuser inlet angle

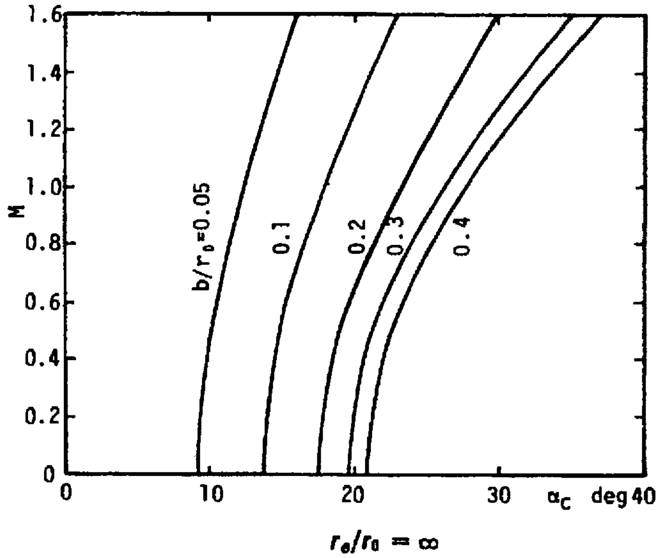

Figure 11: Experimental Results for the Variation of Critical Angle With Inlet Mach Number and Diffuser Height [15]

A secondary problem with a vaneless space where C_θ is large compared to C_r is that the flow path will be long and the flow will remain at high speed for a long time causing high wall friction losses.

Senoo and Kinosita [15] adopted many of Jansen's assumptions, and improved his mathematical model to allow cases where the flow is not symmetrical about the mid plane of the diffuser. Through mathematical models and experiments, Senoo and Kinosita investigated the influence of the ratio of width to inlet radius and found that the critical angle for stall (measured between the flow vector and the tangential direction) was smaller for low blade heights (**Figure 11**).

Therefore lower inlet angles are acceptable for low specific speed stages down to about 10 degrees for b/r=0.05 (although this varies with the other parameters of inlet Mach number, flow asymmetry, Reynolds number, etc). In the discussion Senoo and Kinosita also indicate that reversed flow can be avoided if the vaneless space is kept small (**Figure 12**). The x-axis indicates the inlet angle (between the inlet flow vector and the tangential) and the y-axis indicates dimensionless radial position in the vaneless space, r_0 is the radius of the diffuser inlet. The lines are loci of points where stall occurs for different dimensionless blade heights. The flow through a diffuser for an inlet angle of 10° can be represented by a vertical line and if this line intersects the relevant stall locus then the diffuser will stall (If $b/r_0 = 0.1$ then **Figure 12**, point D shows the position where the stall begins - equivalent to **Figure 10**, point D). Therefore, if the flow enters the vanes of the diffuser at point X then **Figure 12** suggests that the diffuser will not stall for any blade height shown. This point is also shown on **Figure 10**. If the flow enters the diffuser vanes at point X before the point where the boundary layer flow would be tangential (**Figure 10**, point D) then it will be protected from the radial pressure gradient, preventing the stall.

Senoo and Kinosita [15] also investigated tangential variation of the flow where the tangential flow varied from the mean flow by up to 30 percent although the angular period of the distortion is not reported. The distortion had the most effect on diffusers having a high value of b/r_0, and did not have as much effect as radial distortion, however doubts must be raised about whether the flow exiting from an impeller has been accurately simulated.

Jansen [14] measured a high critical inlet angle (to the tangential) for stall for low axial height diffusers, Senoo and Kinosita predict the opposite. Although there is some discussion by Senoo and Kinosita, this disagreement does not seem to have been fully resolved, partly because the experimental setup does not accurately reflect the real inlet conditions of the diffuser of a radial diffuser.

It is also not established that the diffuser does indeed stall when the boundary layer flow reaches the tangential direction. However, it is clear from this discussion

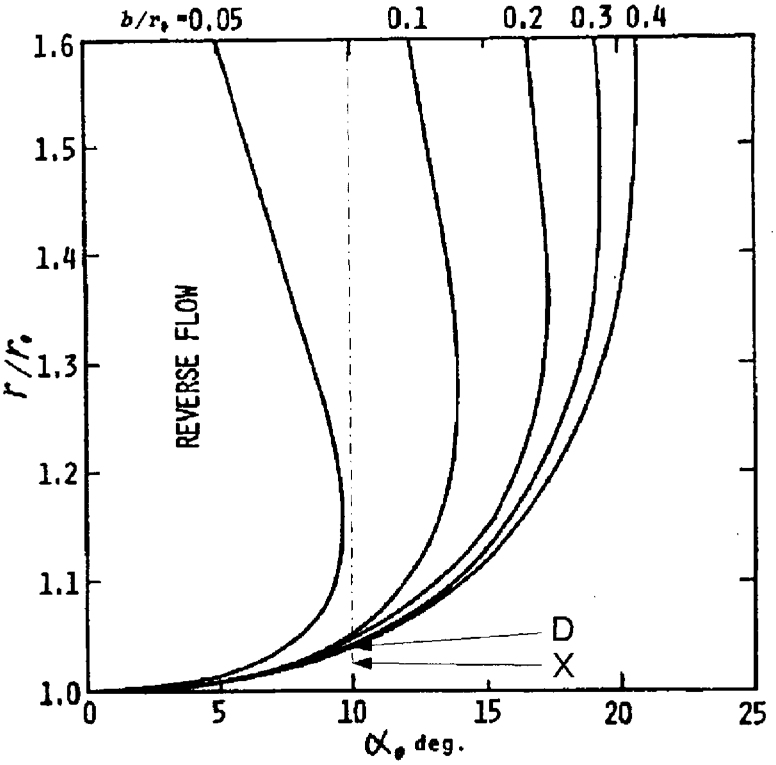

Figure 12: Reverse flow zone of parallel wall vaneless diffusers [15]

that highly tangential flow makes the vaneless space prone to stalling.

1.6.6 No Inducer

Although the reduction of the specific speed causes problems, it also has advantages. In a compressor of an optimum specific speed the flow enters the blades axially and is turned to the radial direction within the rotor. The inlet section of the blades (inducer) is designed to minimise the Mach number at the rotor inlet. In a low specific speed compressor the inlet Mach numbers are relatively low because the rotor is large relative to the volumetric flow (due to the low flow coefficient) and therefore the radial component of the flow is low. The blade speed at inlet is also low, due to the low shaft speed and low diameter of the inlet. Therefore, low specific speed stages have no inducer and are axially shorter. Low specific speed stages are sometimes preferred for this reason as discussed in Section 1.4.

1.6.7 No Ducting Problems

In a compressor of normal specific speed, the high volume flow rate means that very large ducting between stages is required if losses are to be minimised. In a low specific speed compressor, ducts that are of a modest size compared to the machine, can carry the flow at low velocities.

1.7 Comparison of Low Specific Speed Turbomachine Designs

The following section discusses turbo-machines designed to avoid the problems of low specific speed. Four low specific speed compressor stages are introduced and compared. At the end of the discussion, performance parameters are presented in **Table 2**.

The ideal work for any compressor can be calculated from the pressure increase and inlet conditions which can be accurately measured. However, in order to calculate the efficiency, the actual work is also required and this is less straightforward. The power absorbed by a well insulated compressor can be assessed by measuring the temperature change in the gas. This method is less suitable for low specific speed machines because the low flow rate relative to the machine's size cause the machine to act as a heat exchanger, cooling the gas as it is compressed. Under these circumstances, the full temperature rise will not be seen and the isentropic efficiency will be overestimated. Therefore torque measurements are preferred whenever possible.

Two of the compressors presented as described by Rusak [16] and Casey et al [11] are intended for use in the later stages of a multi-stage compressor and therefore it is likely that they were tested at a high inlet pressure (although the inlet pressure is not given). The specification of the gas compressor (to be stated in Section 1.9) requires atmospheric inlet conditions. This would reduce the efficiency loss due to wall friction and windage. It is likely that if these compressors were tested with atmospheric inlet conditions, they would give lower efficiencies. This is discussed further in Section 2.1.3.

1.7.1 Conventional Design methods for Low Specific Speed Stages

Casey describes 4 compressor geometries with varying degrees of backsweep - type A, B, C and D (A, B and C are shown in **Figure 8**). Of these, Build C was found to have the highest efficiency. This is a conventional, high backsweep, low specific speed radial compressor.

The conventional compressor has a low pressure ratio due to the low tip speed necessitated by windage considerations, and the high backsweep. For atmospheric inlet conditions, an estimated 9.9% of the work in this design is consumed by windage.

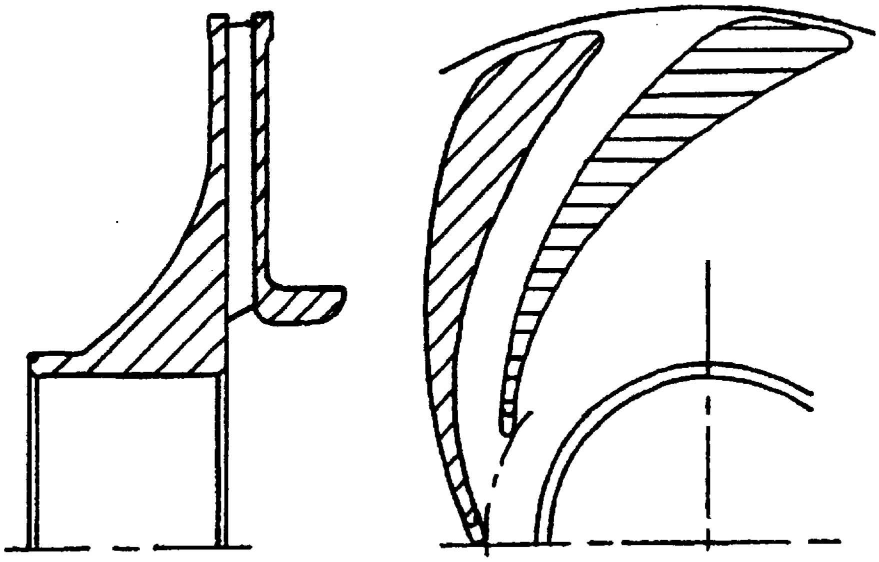

Wedge-type impeller, Impeller A-W

Figure 13: Wedge type compressor [16]

1.7.2 Wedge Type

Rusak [16] proposed a design of low specific speed turbocompressor know as a 'wedge type' compressor, where the blades are very thick and block approximately 70% of the rotor's periphery (**Figure 13**). This allows for a larger hydraulic diameter in the rotor passages; the intention is that the reduction in wall friction will offset the loss caused by large blade wakes. The percentage of the work consumed by windage is particularly high in this design. The radial component of velocity suddenly decreases as the flow leaves the rotor and the loss as the flow turns is inherent in this design. A description of the diffuser is conspicuously absent from the work of Rusak [16] as this part is probably critical. It is not stated whether torque was measured. Efficiencies of 'over 70%' are also mentioned, but detailed specifications are not given.

A higher efficiency than the conventional design would be expected in this case because the volumetric flow is four times greater and so wall friction losses are reduced and the specific speed is greater. The flow coefficient could not be calculated because the data was not given. The tip speed is near sonic and this accounts for the increased pressure ratio.

1.7.3 Barske Type

Rogers [17] attempted to design a compressor that could be driven at the same shaft speed as the gas turbine that it fuelled and developed some unconventional designs originally proposed during the 1940s by Barske [18]. Barske's work seems to have focused on liquid pumps, whereas Rogers' tests were using natural gas, although the design seems to have changed little. Rogers does not report any calculations performed in the design of the pump geometry, and appears to have used a largely empirical approach. The pump consists of a highly scalloped rotor, housed in a volute. The volute only allowed the flow to leave the area swept by the rotor in approximately one sixth of its circumference. Blocking off part of the inlet area with a blanking plate improved performance (**Figure 14**). Large recirculations are inherent in the design and this explains the very low efficiency. Torque was measured in this investigation.

It is not appropriate to calculate the windage percentage for this design because the rotor is so highly scalloped. Although the efficiency is low, the pressure ratio is very high for a single stage machine of this specific speed. The tip Mach number is 1.15 which accounts in part for the high pressure ratio and low efficiency. The specific speed and flow coefficient are very low and so a low efficiency is expected.

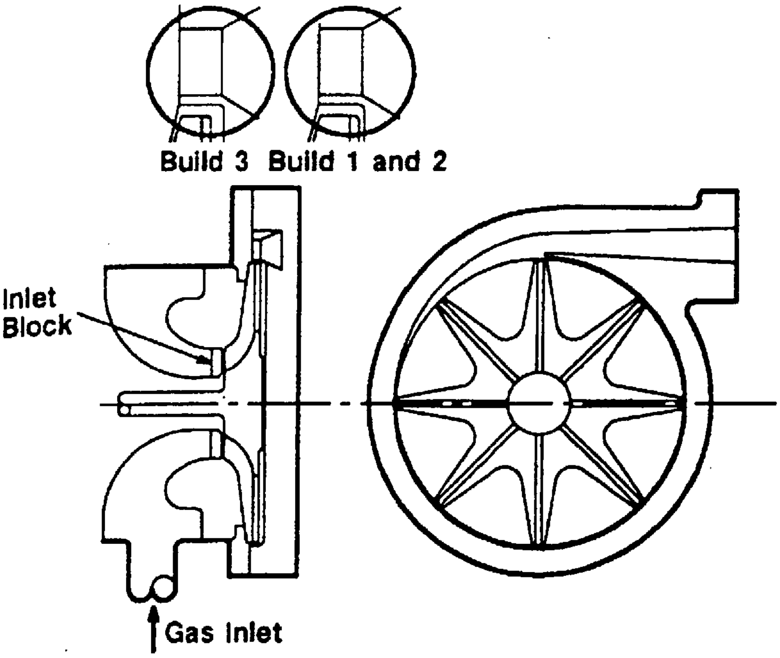

Figure 14: Barske type compressor [17]

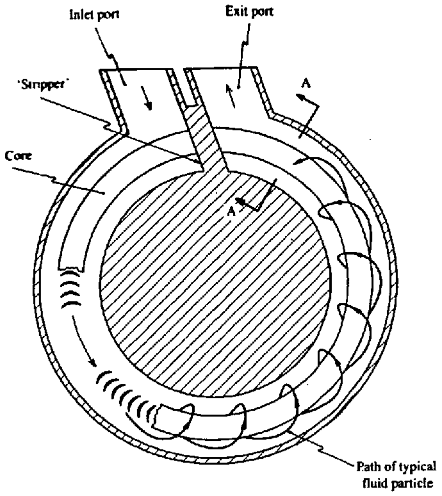

Figure 15: Flow Path in a Regenerative Compressor [19]

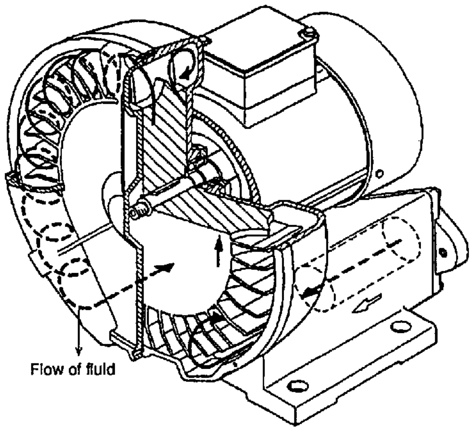

Figure 16: A Regenerative Compressor [19]

1.7.4 Regenerative

The regenerative compressor is an example of a commercially successful turbo-machine of very low specific speed. They have been used in gas turbine fuelling and vacuum applications.

The design consists of a bladed disc in a toroidal channel. The flow path is a toroidal helix. The flow passes through the rotor multiple times gaining energy each time - hence 'regenerative' (**Figure 15** and **Figure 16**). The number of passes is a function of the throttling, rather than a fixed parameter. If the downstream throttling valve is closed completely, the machine will not surge like a conventional turbo-machine, but the gas will continue to circulate in the duct and heat up, but maintain pressure.

The experimental work of Sixsmith and Altmann [20] is quoted in detail by Song et al [19]. Even though the work of Sixsmith and Altmann was carried out in 1977 it appears that design methods have advanced little since then. Song et al claim to present the first analytical compressible flow model to describe the regenerative machine, alongside CFD results. Sixsmith and Altmann measured torque and performed experiments while the compressor was cooled with a water jacket. They therefore report the isothermal efficiency.

The best isothermal efficiency was 57% at a pressure ratio of 1.17 ($N_s = 0.15$). When throttling increased the pressure ratio to 1.5 the efficiency dropped to 44% ($N_s = 0.07$). The isentropic adiabatic work would be 58% of the actual work, but this is not the isentropic, adiabatic efficiency since the compressor was inter-cooled.

The windage is extremely low due to the low tip speed. The efficient range of a regenerative compressor is relatively small, and limited to low pressure ratios (**Figure 17**). Slightly higher performance than that shown in **Figure 17** was achieved by bleeding to and from different locations in the volute. The regenerative compressor is capable of high pressure ratios but at much reduced efficiencies. Sixsmith and Altman [20] have shown that low specific speed machines offer the opportunity to inter-cool effectively due to the large wetted areas. There is no available literature concerning regenerative compressors that have been scaled to very small sizes, presumably because of the efficiency penalty and manufacturing difficulties. This may be a useful field for future study.

As advanced analysis methods like CFD are applied to the regenerative compressor it is possible that its performance can be improved to compete with positive displacement compressors more successfully. A more detailed design study is required to determine whether they could be used in multistage radial compressors. Factors for consideration include the magnitude of additional losses incurred by scaling the

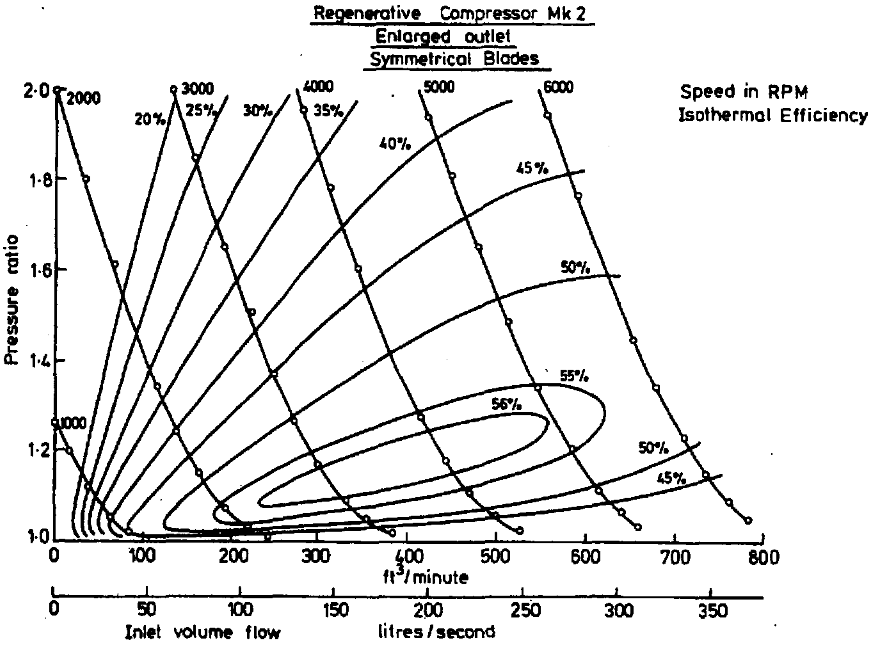

Figure 17: Map of Mk2 Regenerative compressor [20]

Table 2: Comparison of Low Specific Speed Turbo-compressors

	Casey [11]	Wedge [16]	Barske [18]	Regenerative [20]
Specific Speed	0.2484	0.4108	0.0725	0.1000
Flow Coefficient	0.0040	0.0048	0.0015	0.0443
Alternative Spec. Speed	0.1842	0.2900	0.1560	0.0696
Rotor Diameter (m)	0.2500	0.3340	0.2635	0.2820
Estimated Windage %	9.9%	13.7%	-	0.1%
Isentropic Efficiency	50.0%	56.0%	34.5%	-
Pressure Ratio	1.20	1.37	2.31	1.50
Polytropic Efficiency	51.3%	57.9%	39.8%	-
Tip Speed(ms^{-1})	200	347	483	74
Volume Flow(m^3s^{-1})	0.0500	0.1878	0.0512	0.2600

compressor down to the correct size, and whether the specific speed is too low.

1.7.5 Quantitative comparison

The data given for each compressor, including the conventional machine of Casey et al [11], has been compiled to provide a comparison (**Table 2**). The volume flow rate and windage percentage are calculated assuming inlet conditions of 1bar and 300K. The minimum windage was assumed, and this was calculated using the method in Section 2.1.1.

1.8 Conclusions

The need for low specific speed compressors has been established. Conventional turbomachinery is not well suited to low specific speed applications due to high parasitic losses, particularly windage. Either low tip speeds or high windage losses are tolerated in all the designs. Some attempts have been made to improve turbo-compressor performance by developing novel designs, some of which may have advantages for niche markets. Low performance, low specific speed stages are tolerated in multistage compressors for reasons of rotor dynamics; if improvements can be made to low specific speed stages, then they are likely to find use here first. If low specific speed stages were made more efficient, then it is possible that they could replace positive displacement machines in some applications.

1.9 Research Methodology

The original reason for this program of research was to solve the problem of fuel gas compression. The original compressor specification was based on the fuel gas compression application, where the gas compressor would be on the same shaft as the gas turbine. Therefore the shaft speed is fixed by the engine and the flow rate is fixed by the amount of fuel required. This led to the original specification of a shaft speed of 60,000rpm and a flow rate of $10gs^{-1}$. It was considered unlikely that the full pressure ratio of the gas turbine (5.7:1) could be achieved in a single stage and therefore the objective was to minimise the number of stages by maximising the stage pressure ratio while maintaining a competitive efficiency. Air was used as the working fluid rather than natural gas for reasons of safety and simplicity. The pressure of the gas supply is near atmospheric pressure. For simplicity, atmospheric inlet conditions were chosen. The important factor is to develop a design methodology for a very low specific speed turbo-compressor - the exact gas conditions are less important.

However it became clear that the performance of the compressor was much improved at larger sizes. This is due to the lower relative roughness, and finer relative tolerances. The Reynolds number is also higher at large sizes. It was decided to build a rig based on a similar geometry, scaled up by a factor of three to accept nine times the flow rate. This simplified the task of designing a low specific speed compressor as the extra problems of very high quality manufacture and lower Reynolds number flow were not present. The scaled up rig is also more similar to the size of the compressors tested by Casey et al [11] and Rusak [16], and if the inlet is atmospheric then the flow rate is similar to an automotive turbocharger. Compressors of this flow rate may find more applications.

Therefore majority of the analysis and testing presented was performed on the 20,000rpm rig with a design point flow rate of $90gs^{-1}$. Both machines were designed to have an atmospheric inlet. The two specifications are given in **Table 3**.

Table 3: Compressor Specification

Parameter	$60,000rpm$	$20,000rpm$	units
Flow rate	10	90	g/s
Rotor Diameter	70	210	mm
Inlet pressure	101300	101300	Pa
Inlet temperature	300	300	K

It has already been shown that if the inlet to the compressor is atmospheric then windage makes up a large proportion of the losses. Therefore the subject of windage was examined in detail and a method of optimising the windage gap (between rotor and casing) is derived from semi-empirical data from the open literature. It is shown that the windage is extremely sensitive to rotor size, and therefore this must be minimised. In order to achieve the maximum pressure ratio, forward swept rotor blades are used. These are normally avoided because they are less efficient than back swept blades and present problems of stability. However, it is postulated that the saving in windage will be more than the extra mixing out losses at the rotor exit due to the forward sweep. A one dimensional analysis of a compressor based on this principle is presented in Section 2. This is developed into a compressor design.

In the Section 3, the experimental evaluation of a compressor with a design specific speed of 0.19 using a single stage rig at $20,000rpm$ is described.

In Section 4 a CFD analysis of the compressor is described.

Discussion and conclusions of the work follow in Sections 5 and 6.

2 Development of an Innovative Turbo-compressor

In this chapter the novel aspect of the present research is introduced. The windage on a low specific speed compressor can represent a large proportion of the compressor's power. The windage model of Daily and Nece [21] was used to find the minimum windage loss for a simplified case and find the conditions for this minimum. In the light of this, a one dimensional analysis of a low specific speed compressor was undertaken. This is a simplified analysis of the compressor where only the average quantities of the gas are considered and there is no allowance for variation of properties across the width of the rotor or diffuser passage. Consideration of windage at the earliest stage of the analysis, and a need for the maximum pressure ratio leads to a compressor design with highly forward swept rotor blades. Forward swept blades are normally avoided in compressor design and the reasons for this are considered. However for the special case of low specific speed compressors, forward swept rotor blades can be advantageous, and problems associated with forward sweep can be avoided. The consequences of this design in relation to inter-stage leakage and surge resistance are discussed.

2.1 Windage

Windage refers to the action of fluid drag on a rotating object and windage loss refers to the power lost to the fluid by windage. Normally the windage loss for a radial compressor is a very small proportion of the work done by the compressor. However, as the specific speed decreases, the windage becomes more significant [12], implying that a consideration of windage is critical for this subject.

2.1.1 Windage Model - Dailey and Nece

The windage loss is a function of the geometry of the rotor and surrounding stationary components, and the conditions of the fluid. In order to obtain an order of magnitude estimation of the windage loss, it is assumed that the rotor can be modelled as a thin, enclosed disc (**Figure 18**).

The most important research relating to windage is that of Daily and Nece [21] who carried out experiments on the geometry shown in **Figure 18**. Their results have been used to find the conditions that will minimize the energy lost to the fluid by a disc that is similar in size and running speed to a compressor rotor. Daily and Nece assume that the power lost in windage on two sides of a disc can be expressed as:

$$\dot{W}_w = \frac{1}{2} C_m \rho \omega^3 a^5 \tag{13}$$

Where C_m is a coefficient to be determined from experiment. Daily found that there were four flow regimes, each depending on the rotational Reynolds number (Equation 14) and the dimensionless ratio of the axial gap to the rotor radius s/a.

$$Re_\omega = \frac{2a\rho U_{tip}}{\mu} \tag{14}$$

The boundaries of these regimes are shown in **Figure 19** taken from Romero-Hernandez [22]. Regime I consists of merged laminar boundary layers with no radial motion of the fluid, and regime II consists of separate laminar boundary layers, with fluid near the rotor being pumped from small to large radii and fluid near the stationary wall being pumped from larger to smaller radii (by continuity). Regimes III and IV are the turbulent equivalents of these. C_m is calculated differently for each regime

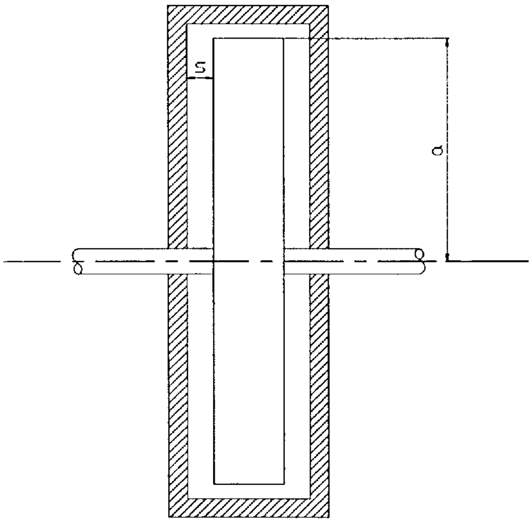

Figure 18: Schematic of enclosed disc

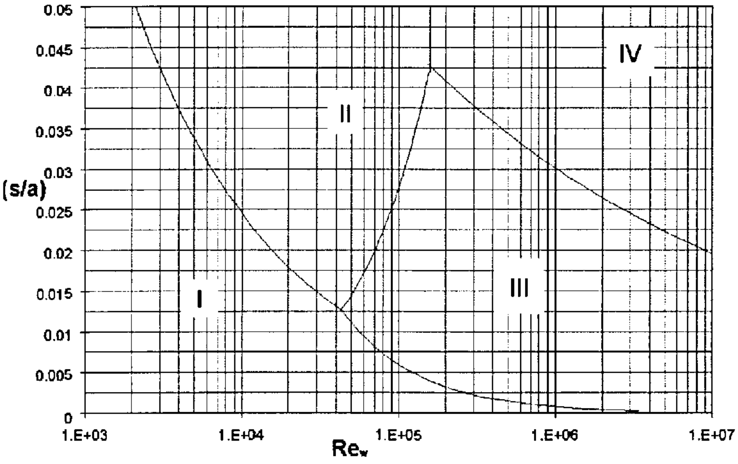

Figure 19: Windage Regimes [22]

Regime I

$$C_{mI} = \frac{2\pi}{\frac{s}{a} Re_\omega} \tag{15}$$

Regime II

$$C_{mII} = \frac{3.7(\frac{s}{a})^{\frac{1}{10}}}{Re_\omega^{\frac{1}{2}}} \tag{16}$$

Regime III

$$C_{mIII} = \frac{0.080}{(\frac{s}{a})^{\frac{1}{6}} Re_\omega^{\frac{1}{4}}} \tag{17}$$

Regime IV

$$C_{mIV} = \frac{0.0102(\frac{s}{a})^{\frac{1}{10}}}{Re_\omega^{\frac{1}{5}}} \tag{18}$$

2.1.2 Evaluation of Windage in the Present Research

If the Reynolds number is greater than 1.1×10^5 and $\frac{s}{a}$ is greater than 0.005 (as it is throughout the present research) then only regimes III and IV need be considered. The minimum value of windage loss for a given radius and speed (i.e. a given Reynolds number) in the region of interest is at the border of the regimes. The minimum value of C_m can be calculated by setting C_{mIII} equal to C_{mIV}. To find the optimum value of $\frac{s}{a}$.

$$\left(\frac{s}{a}\right)_{opt} = \frac{0.402}{Re_\omega^{\frac{3}{16}}} \tag{19}$$

The clearance between the rotor and stator can be chosen by the designer provided that the clearance is large enough to avoid rubbing when the rotor is deflected by vibration. If the optimum gap is chosen then the windage loss for each side can be calculated using equations 13, 18 and 19 combined to give:

$$\dot{W}_w = \frac{0.04656}{Re_\omega^{\frac{7}{32}}}\rho\omega^3 a^5 \tag{20}$$

This formula can be used to calculate the minimum possible windage loss of a simple enclosed rotor of given rotational Reynolds number, providing the following conditions are met

1. The rotor can be approximated to a simple thin enclosed disc (**Figure 18**)
2. Re_ω is greater than 1.1×10^5
3. $\frac{s}{a}$ is greater than 0.005 (calculated from equation 19)
4. s is large enough to make the machine feasible (avoid rubbing).

The real situation is more complex because the actual components are not simple discs and there is often radial flow across the windage surfaces. However this method provides a good estimate of the windage loss. As a rough guide the windage varies with approximately the 4.5th power of rotor diameter at constant shaft speed. A more detailed consideration of windage in a multistage arrangement is contained in [10].

2.1.3 Variation of Windage With Rotational Reynolds Number

In section 1.7 it was stated that windage losses become less significant as the inlet pressure of a given compressor is increased. This can now be shown. Examination of **Equation 20** shows that windage power for an optimised gap is proportional to $\rho Re^{-\frac{7}{32}}$. Assuming that the compressor is operated at the same speed at a higher pressure, and that the viscosity is only weakly dependent on the pressure, the relationship of **Equation 21** is true.

$$W_w \propto \rho^{\frac{25}{32}} \tag{21}$$

Assuming that density is proportional to pressure:

$$W_w \propto P^{\frac{25}{32}} \tag{22}$$

Therefore windage work is relatively weakly dependent on pressure, whereas the ideal work input increases in proportion to increasing pressure. For real compressors, the effect of wall friction in the impeller and stator passages will be slightly reduced at higher inlet pressures due to the effect of increasing Reynolds number. This will cause the work not related to windage to decrease, but this effect is relatively small.

2.2 One Dimensional Compressor Design

The major part of the design of a centrifugal compressor is performed by considering the path of the gas to be one dimensional. During the 1D analysis the rotor size, passage sizes and performance parameters can be calculated. In conventional compressors the empirical data of previous designs can be used to estimate the losses and efficiency of the compressor with reasonable accuracy. This compressor has a low specific speed and an unusual geometry has been generated in order to address the problems associated with this specification. Therefore conventional loss parameters are not appropriate and as a result there is considerable uncertainty in the one dimensional analysis.

As already mentioned, the 1D analysis was originally performed for the 60,000rpm rig, although it has been scaled to 20,000rpm for clarity. The 1D design presented here was influenced and refined on the basis of the results of CFD simulations (discussed in section 4).

The mass flow rate of the compressor is already fixed by the specification. In order to begin, the shaft speed was also fixed at 20,000rpm (originally 60,000rpm). The speed of 60,000rpm was chosen because it was originally intended to drive a fuel gas compressor on the same shaft as the gas turbine engine.

Preserving a good blade height was seen as important in developing an efficient machine. For compressor "C" described by Casey et al [11], the blade height was 2.7% of the rotor diameter which would be 1.7mm for 60,000rpm. The blade height for this design was originally set at 3mm which was considered the minimum height for which a reasonable efficiency could be expected. For simplicity this is kept constant throughout the machine. The blade height became 9mm after scaling.

The rotor diameter was the next important parameter. If the shaft speed is kept constant and the windage gap is always optimized then the windage loss varies with the 4.5th power of radius. The specific power transferred to the main flow of gas varies with the square of the radius (because C_θ is normally proportional to the rotor tip speed). This explains why either high windage losses or low tip speeds are tolerated in low specific speed machines.

Windage can easily dominate a low specific speed machine so the proportion of work consumed by windage was set at 2.5%, resulting in a lower tip speed than in conventional turbo-machinery. Choosing a small rotor also helps to increase the flow coefficient, which means that problems of low hydraulic diameters are less likely. At this stage it was not known how much work the compressor would do, so the rotor diameter was set at 250mm as a first guess. This size is similar to the rotors of Casey et al [11], but will eventually be adjusted so that the windage work is 2.5% of the total work. In order to make a more informed choice for the rotor size, it would be necessary to also know how aerodynamic losses and head coefficient varied with rotor size. Increasing the rotor size would not only increase the windage, but also increase the aerodynamic losses due to the greater wetted area. It would also decrease the radial speed at the rotor exit which is already small. Decreasing the rotor size would reduce the pressure ratio, and therefore reduce the specific speed. This would lead to an excessive number of stages for a given specification.

In order to calculate the work of the compressor, the blade speed and the absolute tangential rotor exit speed ($C_{\theta 2}$) must be fixed. With the rotor diameter and shaft speed defined it is possible to calculate the blade speed. An objective of this design is to maximise the pressure ratio at good efficiency as discussed in section 1.6.2.

$$\dot{w} = U_2 C_{\theta 2} - U_1 C_{\theta 1} \tag{23}$$

The Euler turbo-machinery equation is derived by considering the torque produced by the momentum change of the gas as it passes through the rotor, and inferring that the product of this torque and the rotational speed is equal to the work input of the machine (**Equation 23**). If the gas enters the machine radially the Euler turbo-machinery equation reduces to **Equation 24**.

$$\dot{w} = U_2 C_{\theta 2} \tag{24}$$

This shows that the work transferred to the gas is proportional to the tangential gas speed as it leaves the rotor. However as the gas reaches sonic speed, shock losses become important. Therefore the tangential exit speed should be as high as possible without the gas speed reaching the speed of sound. It is not possible to calculate the Mach number at this stage as the rotor exit temperature is not known, so a speed of 305m/s will be used (equivalent to Mach 0.9 at standard conditions). The total speed also has a radial component but this is small due to the low flow coefficient and therefore has a negligible effect on the total speed. The work can now be calculated, and the windage can also be calculated using the method explained earlier. The rotor size is adjusted to 210mm in order that windage represents 2.5% of the total work. It should be noted that the blade speed is less than the absolute gas speed, implying that the blades are forward swept rather than backswept as in conventional compressors. Normally such an unusual design would not be considered, partly because it is so different from conventional designs. There are two potential reasons why the compressor might be expected to stall easily and therefore have a poor range: highly tangential flow at the diffuser inlet, and the risk of giving the compressor characteristic a positive gradient. Both of these problems are addressed in 2.3.2. The parameters calculated so far are shown in **Table 4**.

Table 4: Compressor Parameters

Parameter	Value	Units
Mass Flow Rate	0.09	kgs^{-1}
Blade Height	0.009	m
Rotor diameter	0.21	m
Rotational Speed	$20,000$	rpm
Angular Frequency	2094	$rads^{-1}$
Rotor Tip Speed	219.9	ms^{-1}
$C_{\theta 2}$	330	ms^{-1}
Total Power	6531	W
Windage Power	354	W
Windage Percentage	2.3	%

In order to calculate the pressure ratio, it was necessary to define some more parameters. The overall efficiency of the compressor was guessed, and the inlet temperature and pressure were chosen as shown. The temperature rise, exit temperature, and pressure ratio were calculated (**Table 5**).

Table 5: Compressor Parameters

Parameter	Value	Units
$\Delta T_{1,3}$	72.2	K
T_3	402.2	K
Overall Efficiency	60	%
Isentropic Temperature Rise	43.32	K
T_1	300	K
P_1	101300	Pa
P_3	162427	Pa
Pressure Ratio	1.60	-

2.2.1 Passage Sizing

In order to complete the first attempt at a compressor design, the sizes of the passages must be calculated. The aerodynamic blockage of the passages is not known, it was estimated on the basis of CFD performed at an early stage of the project. In order to calculate rotor exit conditions, it is necessary to work back through the machine from the diffuser exit. Stagnation conditions are assumed at the diffuser exit.

A Mach number of 0.2 is chosen for the air at the exit of the diffuser because at this speed it will have very little kinetic energy. This allows the correct size for the diffuser exit to be calculated. In calculating the gas conditions throughout the diffuser it is necessary to take account of losses in the diffuser. The static to static efficiency is used as this is a measure of the diffuser's ability to recover static pressure. Because of the high rotor exit flow angle, a vaneless diffuser cannot be used. Therefore the diffuser consists of a scroll-like section which comes to a throat, and then continues as a more conventional divergent duct. In the manufactured design, the duct is curved to reduce physical size (**Figure 21**). The loss for the diffuser is therefore split into two sections, the scroll section, and the duct section, each with its own static to static efficiency. Conditions at the throat can be calculated from the compressor exit conditions and the duct efficiency **Table 6**.

Table 6: Compressor Parameters

Parameter	Value	Units
Diffuser Exit Mach	0.2	-
No. Diffuser Passages	4	-
Diffuser Exit Speed	77.34	ms^{-1}
Exit Density	1.520	kgm^{-3}
Exit Blockage	0.75	-
Exit passage width	0.0283	m
Duct Effectiveness	0.8	-
Throat Mach	0.7	-
Throat T	388.99	K
Throat Speed	258.34	ms^{-1}
Throat P	124717.7	Pa
Throat row	1.28	kgm^{-3}
Throat blockage	0.75	-
Throat width	0.0100	m

Initial CFD showed that the significant diffusion in the scroll in this design was beneficial. The Mach number at the rotor exit will now be calculated by iterating to find the rotor exit temperature. In order to do this a first guess for the rotor temperature is required (the radial speed must also be guessed, but the tangential speed differs in magnitude from the total speed by less than 0.2% since the radial speed is small by comparison). The Mach number at rotor exit is then calculated from the speed and the temperature conditions. This enables an improved guess of the temperature based on the stagnation conditions and the Mach number. This is used to update the initial guess until the values agree (**Table 7**). The overall efficiency, and the loss measures already given imply a rotor total to total efficiency of 81%.

Table 7: Compressor Parameters

Parameter	Value	Units
Rotor exit T	317.8	K
Radial Speed	14.13	ms^{-1}
Rotor Exit speed	330.46	ms^{-1}
Rotor Exit Mach	0.925	-
Scroll Effectiveness	0.6	-
Rotor Exit P	108751.7	Pa
Rotor Exit Density	1.192	kgm^{-3}
W_{r2}	14.13	ms^{-1}
$W_{\theta 2}$	110.09	ms^{-1}
W_2	110.99	ms^{-1}
Rotor Exit Density	1.19	kgm^{-3}

The inlet passage sizes were calculated in a similar manner and the rotor and diffuser were designed on the basis of this analysis. **Figure 20** shows a conventional compressor for comparison with the new design, shown in **Figure 21**.

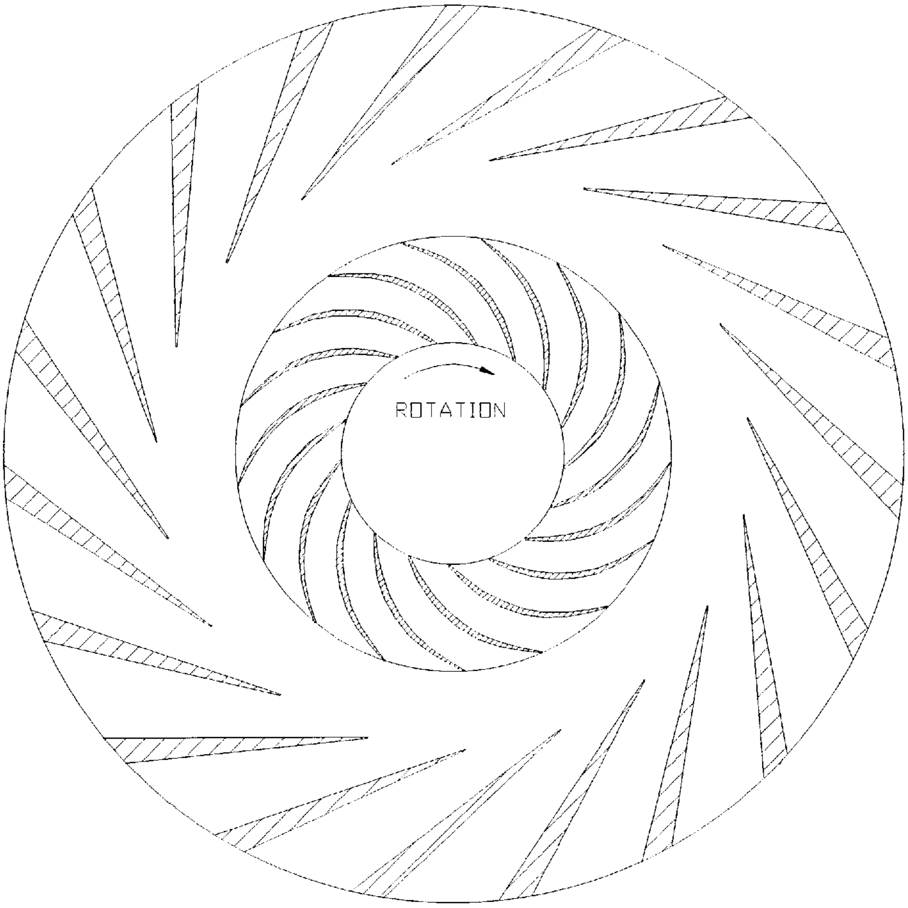

Figure 20: Conventional compressor design

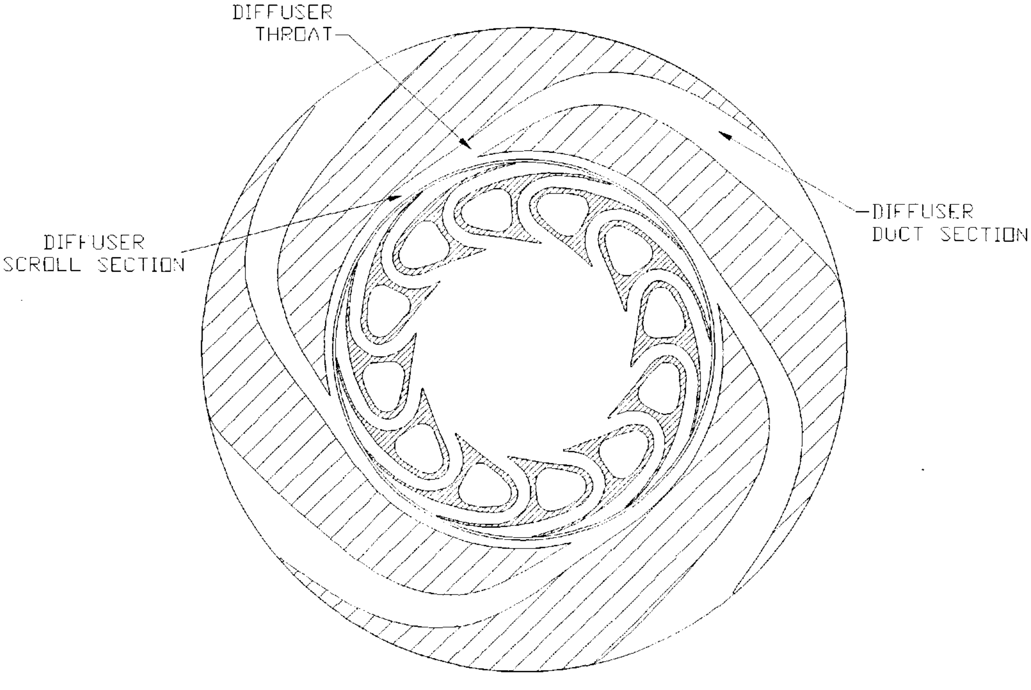

Figure 21: Novel compressor design

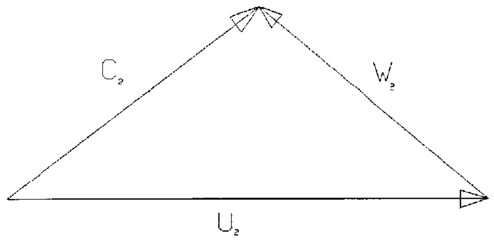

Figure 22: Conventional Velocity Triangle

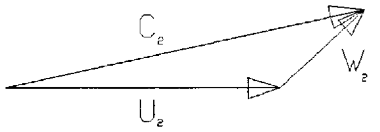

Figure 23: New Design Velocity Triangle

2.3 Consequences of forward swept design

Figure 22 and **Figure 23** compare a normal compressor rotor exit velocity triangle with that of the new design. The flow angle is particularly large, this is due to the low meridional velocity. At this stage of the analysis it was unknown whether it was possible to achieve very high speed, highly tangential flow. This question will be addressed in the experimental and computational work in the rest of this thesis. In this design the flow leaving the rotor is guided by both the rotor blades and the diffuser and therefore it is also difficult to predict accurate values of slip so that the blade angle can be defined (until now only the gas flow vector has been discussed). The design proceeded with the best estimates available and in future, data from a detailed examination of this design will be used to improve subsequent designs.

2.3.1 Blade loading

Blade loading is defined as the ratio of pressures on the pressure and suction sides of the blades. Backsweep is beneficial because the centrifugal force increases the pressure on the suction side and decreases the pressure on the pressure side, thus unloading the blades. This is particularly important at the rotor exit where the air following the pressure and suction side must mix at the trailing edge. Most designs reduce loading to a minimum at the trailing edge for this reason. In the forward swept design it is difficult to reduce the loading at the trailing edge and therefore mixing out losses will be greater. The hypothesis of the present research is that the reduction in windage for the forward swept design, together with the reduction in passage losses due to the increase in blade height, will be greater than the increase in mixing losses.

2.3.2 Stability

Forward swept compressors frequently suffer from instability - they are not frequently used as they generally have a small range before surging. An explanation of this is given by Cumpsty [6].

If a compressor is followed immediately by a throttling valve then it will surge when the gradient of the operating characteristic of the compressor exceeds that of the throttling valve. At point B in **Figure 24** the compressor is stable because although a small decrease in mass flow will cause a decrease in the pressure rise of the compressor, it will cause a greater drop in the ΔP of the valve and therefore equilibrium will be restored. At mass flows less than that of point A the compressor will not exhaust any flow because it cannot overcome the pressure drop of the valve and will therefore surge.

However if the compressor exhausts directly into a plenum without any momentum in the flow, then the compressor will surge when the gradient of the compressor characteristic becomes negative (at point C) because a small decrease in flow rate will cause a lower pressure at the compressor exit than is in the plenum and the gas will be accelerated backwards through the compressor.

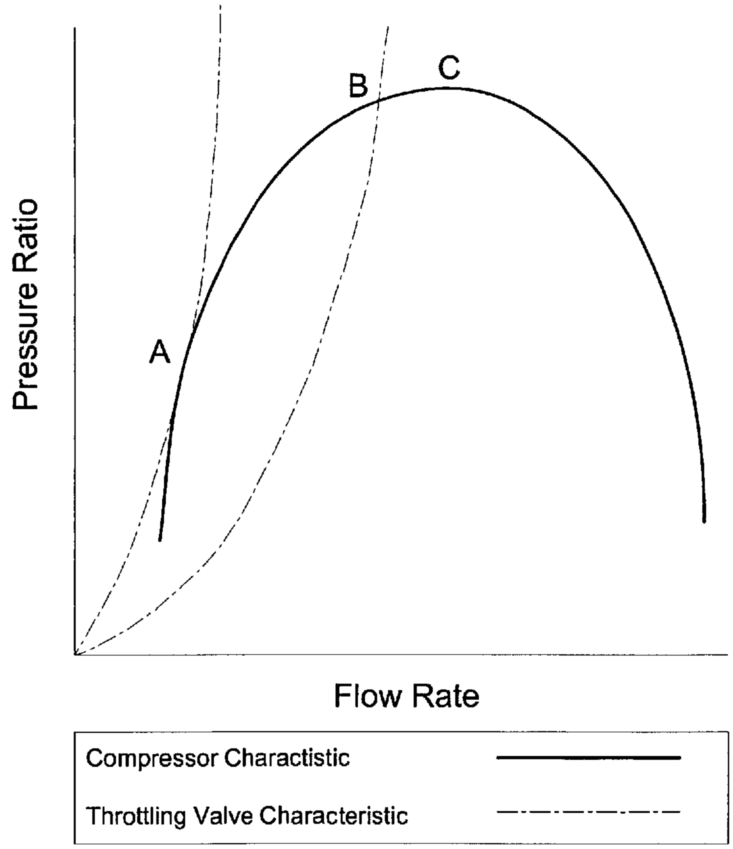

Figure 24: Compressor immediately followed by a throttling valve

In the case of a back swept compressor, a decrease in flow rate will cause an increase in absolute tangential velocity, causing an increased pressure ratio, and hence backswept compressors are inherently stable. Conversely, forward swept compressors are inherently unstable. However forward swept compressors can be made stable by losses in the diffuser when the extra pressure produced by an increase in mass flow is wasted by increased wall friction, and poor incidence.

In the forward swept compressor, an increase in flow rate causes an increase in specific work, and this increase must be wasted in order to prevent the gradient of the characteristic from being positive. The relative velocity increases proportionally to the flow rate. However since the relative velocity is small compared to the absolute velocity, the absolute velocity does not change greatly. In this design total velocity and the tangential velocity are almost identical because the radial velocity is negligible. **Table 8** shows the effect of three different flow rates between 70 and 105 g/s. A 50% increase in the flow rate causes a 15% increase in the absolute velocity and therefore to the specific work. At the high flow rate only 15% of the ideal work input must be wasted for the compressor to remain stable.

Table 8: Variation of absolute rotor exit speed with flow rate

Flow rate (gs^{-1})	Relative Speed (ms^{-1})	Absolute Speed (ms^{-1})
70	101	320
90	130	350
105	150	370

In order for the diffuser to stablise the compressor it does not have to be lossy at all operating points, it merely has to dissipate whatever increase in pressure rise there is as a result of an increase in mass flow rate. In this case the rate of increase in pressure rise with mass flow rate is relatively small. Therefore the compressor can theoretically be very efficient on the surge line, and then become less efficient, but only marginally, as the mass flow rate increases.

In the highly forward swept design, changes in flow do not affect incidence greatly as the flow is always virtually tangential. However, low specific speed machines generally have high wall friction, and in this case it is useful in stabilising the compressor. The gas speeds in the diffuser are higher in this design than in conventional low specific speed machines so it is not surprising that the diffuser can stabilise the compressor.

2.3.3 Diffusion

In a standard radial compressor, the amount of diffusion (pressure recovery) which occurs in the rotor is a key parameter. It is useful to increase the static pressure throughout both the rotor and the stator to allow a gradual, smooth and therefore efficient compression. However, in the forward swept design, it is undesirable to recover kinetic energy as static pressure. The forward swept design relies on the gas leaving the rotor at high speed so that work can be transferred to the gas (as expressed in the Euler turbomachinery equation - **Equation 23**). If the speed of the gas dropped then the pressure ratio would be reduced.

In a backswept compressor the opposite is true. If the pressure recovery is increased reducing the speed in the frame of the rotor, then the speed in the absolute frame will increase. Furthermore, in backswept compressors, extra diffusion in the rotor is often achieved by decreasing the backsweep and making the blades more radial (**Figure 25** and **Figure 26** show the changes in passage width of a radial and backswept compressor. The passage width is indicated by circles). This increases the pressure ratio by increasing the tangential component of the rotor exit velocity. Making the blades more radial in the forward swept case would decrease the pressure ratio. Therefore diffusion in the rotor should be kept to a minimum in the new design.

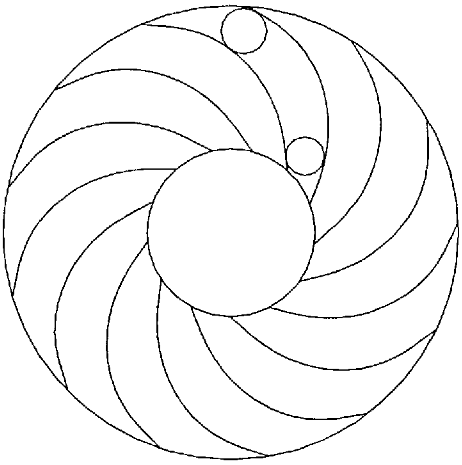

Figure 25: Compressor 1

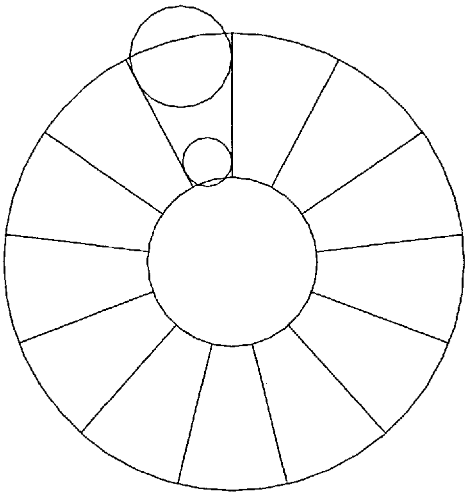

Figure 26: Compressor 2

2.3.4 Leakage

Most low specific speed compressors are shrouded as the prevention of blade tip leakage is critical (Section 1.6.1). Shrouds are prohibited by stress problems in compressors with high tip speeds, but this problem is not encountered in low specific speed rotors. However there can still be significant leakage over the shroud seal, driven by the static pressure rise in the rotor. A useful consequence of the low pressure recovery in the rotor is that at the rotor exit, the static pressure is similar to the inlet, as the energy added to the gas by the rotor is seen in kinetic energy rather than pressure rise. This reduces the driving force for leakage across the shroud which is a key concern for low specific speed machines.

2.4 Conclusions

The minimum windage on a simple disc can be calculated as shown in this chapter. Windage work varies with the 4.5th power of radius at constant shaft speed (approximately) whereas work increases with the square of radius and therefore windage can easily become the dominant loss mechanism at low specific speeds. This provides a powerful incentive to reduce the rotor size. In order to maximise the pressure ratio, a rotor design with forward swept blades is proposed. In the new design it is intended that the windage should account for a small percentage of the compressor total work (approximately 5%). The mixing out losses are likely to be higher than in a conventional low specific speed stage, but it is thought that this will be more than made up for by the reduction in windage. It is intended that this should lead to a more efficient design. Normally stability is a problem with forward swept compressors, however it may be possible to avoid these problems with careful diffuser design.

3 Experimental Investigation

3.1 Introduction

This section describes the experimental evaluation of the compressor designed in Section 2 based on high forward sweep. The design specific speed of the compressor was 0.19, and the shaft speed was $20,000 rpm$.

It was planned that a torque sensor could be used to determine the shaft work, avoiding the energy balance method. However the torque sensor was found to be inadequate, and therefore the energy balance method was used. Inlet and exit pressure and temperature were measured in order to determine the pressure ratio and efficiency. Since the static temperature was measured at the exit, a correction must be applied in order to determine the total pressure and this increases the uncertainty. A consequence of the low specific speed of the compressor is that the power of the compressor is low compared to conventional designs of this physical size. Therefore it has a greater tendency to loose heat to its surroundings. The heat lost must be assessed in order to calculate the correct power input. Because the heat loss is greater than 5% of the shaft power, the compressor cannot be considered nearly adiabatic. Therefore the efficiency is referred to as the non-adiabatic efficiency.

The compressor achieved a pressure ratio of 1.52 at an efficiency of 49% ± 3.1 percentage points. The measurement of torque should be pursued as it is considered technically feasible due to the low shaft speed.

3.2 Experimental Compressor Test Rig

The compressor designed in Section 2 was built and experimentally evaluated. The design specific speed was 0.19, the design flow coefficient was 0.0077 and the design head coefficient was 0.90.

The rig has a maximum shaft speed of $20,000rpm$, which allows it to be belt driven from a standard motor with a nominal speed of $3000rpm$ through a variable speed inverter. Driving a conventional compressor for this flow rate would be more difficult due to the high shaft speed. The low running speed also means that a rotary torque meter can be used to measure the shaft work instead of calculating the work input from the total temperature rise between inlet and exit. A lay shaft was used for the belt drive in order to isolate the radial bearing loads caused by the belt from the compressor.

A section view of rig C is shown in **Figure 27**. The bearings are spring preloaded. This method is superior to simply clamping the bearings because the preload is unaffected by thermal expansion of the rig. An axial flow shaft seal was used to prevent leakage past the back-face of the compressor rotor. The clearance for the shroud seal was set by measuring all the relevant parts and calculating the correct size for the seal to achieve the required clearance. Abradable seal pads were used so that close clearances could be maintained, and if the seal knives did touch the casing then this would not be catastrophic. Inlet conditions were measured at Station 1 and exit conditions were measured at Station 3.

The rig was designed to allow further investigation as the front plate is clear of instrumentation fittings so that visualization techniques or further detailed instrumentation can be fitted, although this was beyond the scope of this project.

Downstream of the compressor, a valve was used to vary the back pressure on the compressor and thus control the flow rate.

3.2.1 Instrumentation

Vibration was monitored during the test using a velometer and interpreted by a fast Fourier transform computer. This is required for safety as it gives early warning of

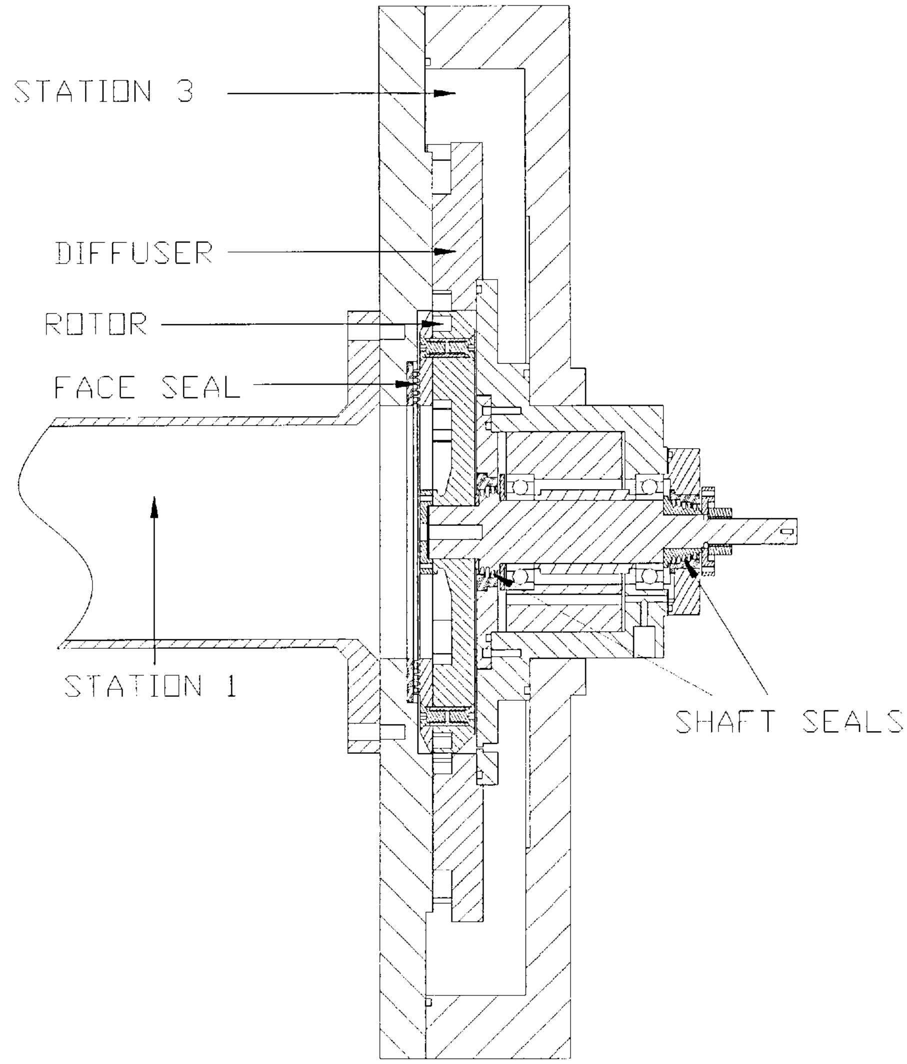

Figure 27: Compressor Test Rig - Section View

problems such as rubbing and high out of balance.

Silicon diaphragm pressure transducers were used throughout the tests. The sensors use only two wires to carry their power and signal and give a 4 to $20mA$ current signal.

Platinum resistance thermometers (PRTs) were used for temperature measurements. Head mounted current transmitters translated the voltage to a current signal representing temperature. The minimum insertion depth of 50mm was observed.

A vortex type flow meter was used to measure volume flow rate, and this data together with the temperature and pressure were used to calculate the mass flow. The flow meter was a Trio-wirl S FS4000 flowmeter, manufactured by ABB [23]. The principle of operation is explained by Dijstentelbergen [24]. The fluid is swirled by vanes near the inlet, and then passed through a duct that converges to a throat and then diverges. The fluid leaves the throat in a swirling jet which precesses around the pipe. The frequency of precession is proportional to flow rate over a wide Reynolds number range. The frequency of precession is measured by a pressure transducer. The flow meter gave a current signal as its output. It would have been possible to measure mass flow directly using a hot film flow meter, but such flow meters are prone to fouling and therefore are not preferred.

Data was collected using a National Instruments data acquisition card (6034E) and a computer. This card uses accurate analogue to digital conversion to convert voltage signals into data that can be processed by the computer. Data was sampled once a second. Accurate resistors were added to 8 of the 16 channels in order to change the channels from voltage to current sensing channels. Sensors with a 4-$20mA$ output were used where ever possible because of their immunity to noise and contact resistances. Screened, twisted pair cable was used throughout.

A thermocouple was used to measure bearing temperature, as a fast response was more important than high precision.

Figure 28 shows a photograph of the rig and instrumentation.

A rotary torque meter was designed into the rig. The torque meter works by measuring the strain of the shaft by two surface acoustic wave devices. These devices generate acoustic waves by electric stimulation of a piezoelectric crystal. When the crystal is strained, the generated frequency changes, and this change can be measured. The mountings for the torque meter were designed after consultation with the manufacturer. It was mounted in a housing located by flanges to preserve concentricity. The torque meter had its own bearings and therefore flexible couplings specified by the manufacturer were used in order to cope with any misalignment between the torque meter, the layshaft and the compressor.

Although it failed to measure torque correctly, it measured the speed correctly. The speed of the motor was set by the inverter, and checked against the fundamental vibration frequency measured by the velometer.

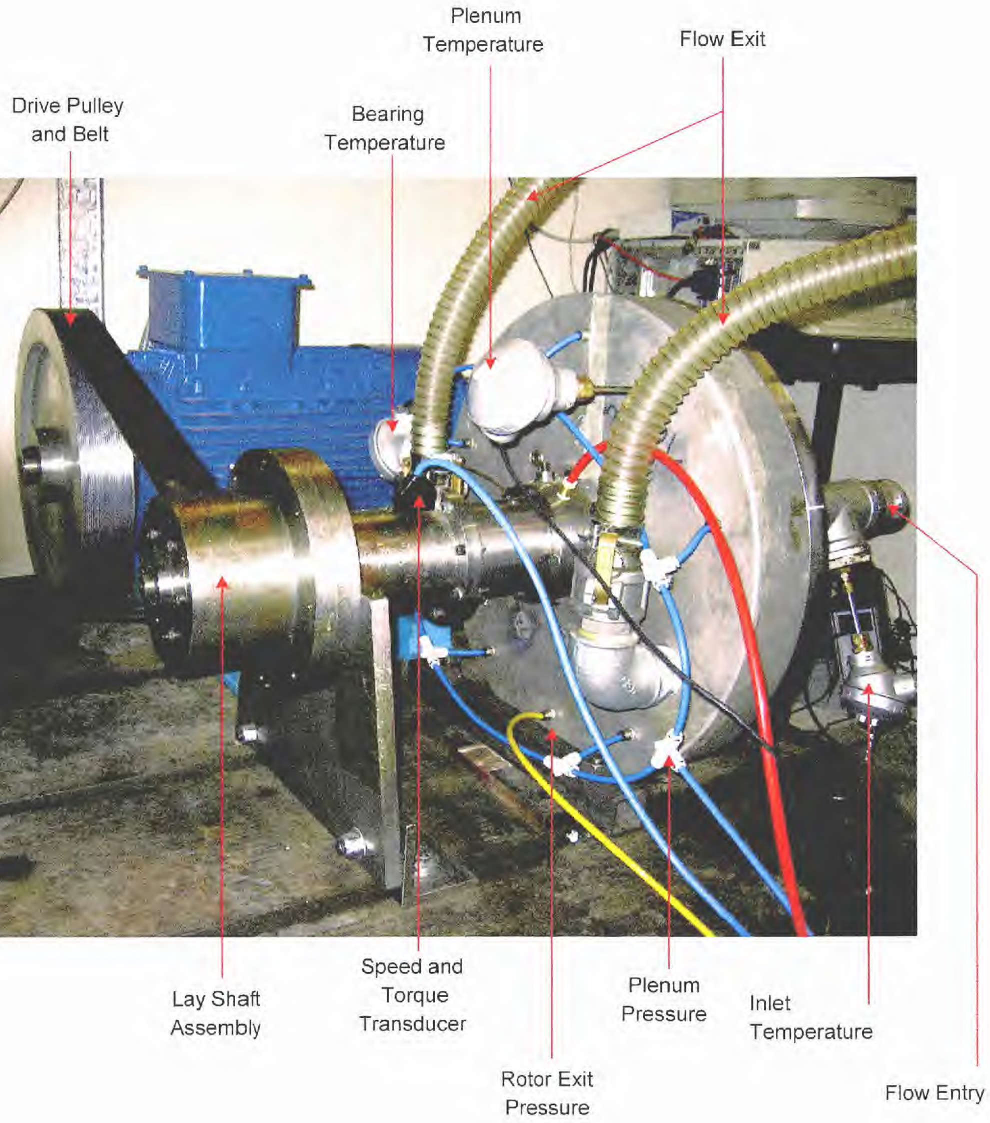

Figure 28: Low Speed Rig and Instrumentation (insulation removed)

3.3 Test Procedure

Before each test run the atmospheric pressure was recorded and the gauge sensors were adjusted to zero.

In order to obtain the performance of the compressor for an operating point, the compressor must reach thermal equilibrium. For each operating point, the casings of the compressor must reach equilibrium with the gas exiting the compressor. Initially the casings are cold and the gas is hot, so the gas is cooled by the casings and the efficiency is overestimated. The temperature for a given speed and exhaust valve position rises as the casings heat up and lose their capacity to cool the gas. A state of equilibrium is reached when the amount of energy transfered between the gas and the casings is the same as the amount of energy lost from the casings to the surroundings. The temperature of the gas under these conditions is constant. In the tests the criterion for equilibrium was that six readings taken over a ten minute period should not vary more than $0.5°C$. This criterion was observed throughout the tests.

In order to traverse the map, the speed of the compressor and the valve position were varied.

3.3.1 Heat Loss

The heat loss from the compressor must be quantified for two reasons. Firstly to determine if the heat loss is small enough to consider the difference between the real process and the adiabatic process to be negligible. This is the case if the heat loss is less than 5% of the input power. If this is the case then the calculated efficiency can be referred to as the isentropic efficiency. Secondly to calculate the correct input power. The input power will be underestimated if calculated from the change in total temperature between inlet and exit in the presence of heat loss. Therefore to calculate the correct value for input power, the power lost as heat must be added to the power indicated by the change in total temperature to determine the total input work. If the heat loss is greater than the required accuracy of the work input, it will be necessary to make this correction even if the real process is near adiabatic.

The heat loss will be calculated, then the efficiency will be calculated using an isentropic compressor as a reference for the ideal work. If the heat loss is less than 5% the efficiency will be the isentropic efficiency.

In order to determine the heat transfer during the tests, the rig was left to cool from $70°C$ after testing, and the cooling curve was recorded. The temperature in the plenum was measured. This temperature is assumed to indicate the casing temperature due to the long times involved when the air within the plenum can reach the casing temperature. The ambient temperature in the test cell was measured at the start of the test run using an additional PRT.

An exponential function was fitted to this curve such that the rate of cooling could be determined for a given temperature. The heat loss could then be calculated from the thermal mass of the rig. The compressor temperature variation with time is assumed to have the form of **Equation 25**.

$$T - T_{inf} = (T_o - T_{inf})e^{ct} \tag{25}$$

Where T is the temperature at time t, T_o is the starting temperature, T_{inf} is the temperature of the surroundings, and c is a constant. Taking natural logs of both sides:

$$ln(T - T_{inf}) = ln(T_o - T_{inf}) + ct \tag{26}$$

This is analogous to the equation of a straight line:

$$y = c + mx \tag{27}$$

So if the log of temperature difference is plotted against time, the gradient will give the constant c. **Figure 29 and 30** show the resulting curves overlaid on the experimental data. The fitted curves show a good correlation to the data, the value of c is -5.9×10^{-5}. The cooling test was repeated and the value of k varied by less than 2%.

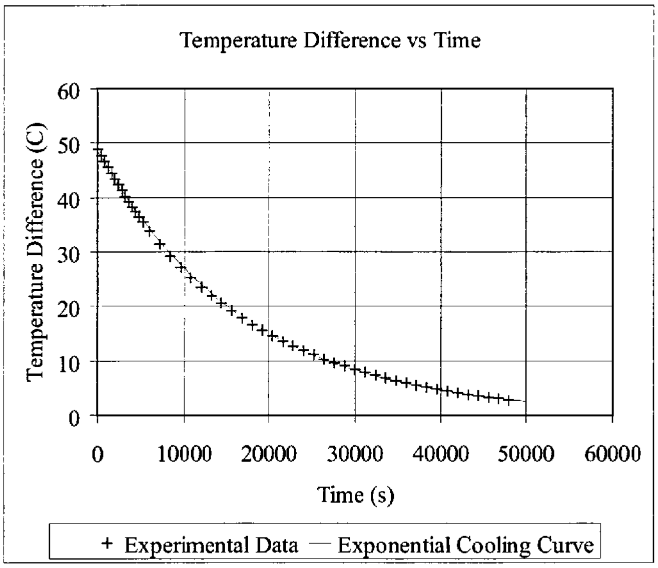

Figure 29: Experimental Data and Cooling Curve

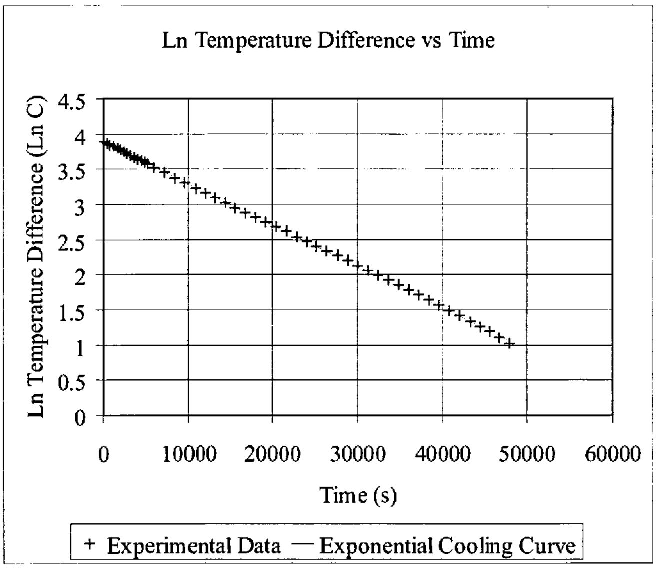

Figure 30: Linear Relationship Between $\ln(\Delta T)$ and Time

The constant c can be used to calculate the cooling rate for a given temperature. If **Equation 25** is differentiated with respect to time it yields an expression for cooling rate in terms of the temperature difference (**Equation 28**).

$$\frac{dT}{dt} = (T_o - T_{inf})ce^{ct} \tag{28}$$

Substituting **Equation 25** yields:

$$\frac{dT}{dt} = c(T - T_{inf}) \tag{29}$$

For a cooling mass, the heat loss is given by

$$\dot{Q} = \frac{dT}{dt}mc_p \tag{30}$$

The rig is made from more than one material so mc_p must be calculated for each component and summed. The cooling rate is known from **Equation 28** and can be substituted into **Equation 30** to give **Equation 31**.

$$\dot{Q} = c(T - T_{inf})\sum mc_p \tag{31}$$

The density and heat capacity of the materials are known and the volume of each component can be calculated using the 3D design package used to design the rig (Pro-Engineer). The sum of mc_p for all the components was $72000kgJK^{-1}$. The rig was bolted to a steel base plate which was slightly warmed by the heat of the rig during the tests. With the rig at $70°C$ the base underside of the base plate where the rig was bolted reached $35°C$ (ambient temperature was $20°C$). A few centimeters from the rig, the base plate was at room temperature. It is unclear the extent to which this mass contributes to the rig's thermal mass. Therefore a section of the base plate the size of the rig's footprint will be added as an uncertainty in the heat loss. The thermal mass of this section of the base plate was $30000WsK^{-1}$. Therefore the thermal mass of the rig is determined to be $(87000 \pm 15000)WsK^{-1}$. Since the heat loss is a small proportion of the energy input to the rig, the large error band will not be reflected in the final efficiency error.

The ambient temperature was measured at the start of the test and the difference between this and the plenum temperature was used to find the heat loss. During the tests the casing was heated by the air. While the casing was heating up, the air temperature in the plenum slowly rose until a steady state was reached. Therefore for each data point, it was required to wait until the plenum temperature drift was less than $0.5°C$ over 10 minutes. At this point it is assumed that the plenum temperature reflects the casing temperature.

The heat loss measured by this method was up to 400W, which represented up to 15% of the shaft power, although at speeds above 15000rpm it was less than 10%.

In service the maximum temperature was $90°C$. As the rig slowed down from full speed, enough cold air blew through the rig to cool it to 70 degrees. Extrapolation to $70°C$ temperature difference for the calculation of heat loss is considered appropriate since the data fits the model well.

3.4 Data Processing

The pressure, the temperature, and the volumetric flow rate were measured by electrical sensors, which gave a current signal as their output. In the following section, the error in measuring a general quantity Q using a sensor producing a current signal is discussed. Expressions generated for the general quantity are applied to find errors in temperature and pressure. Further error analysis follows in order to combine the errors in directly measured quantities to give errors in efficiency, mass flow rate, and pressure ratio.

The current given by the sensors varies between 4 and $20mA$ and is a linear function of the quantity being measured. The quantity can only be measured within the limits of the sensor - between the maximum and minimum values of the quantity: Q_{max} and Q_{min}. The full scale deflection of the sensor r_Q is

$$r_Q = Q_{max} - Q_{min} \tag{32}$$

and the range of the current is given by

$$r_I = I_{max} - I_{min} \tag{33}$$

In this case $r_I = 16mA$ and$I_{min} = 4mA$. **Equation 34** was used to convert the measurement from a current to a quantity.

$$Q = \frac{r_q}{r_I}(I - I_{min}) + Q_{min} \tag{34}$$

The error in a quantity Q is given by the sum of the error caused by the sensor measuring the quantity and converting it into a current (ΔQ_{sen}), and the error in measuring the current (ΔQ_I).

$$\Delta Q = \Delta Q_{sen} + \Delta Q_I \tag{35}$$

The current is calculated using **Equation 36**

$$I = \frac{V}{R} \tag{36}$$

The error in measuring the current is given by

$$\frac{\Delta I}{I} = \frac{\Delta V}{V} + \frac{\Delta R}{R} \tag{37}$$

The error in Q resulting from the error in the measurement of the current is:

$$\Delta Q_I = I\frac{r_q}{r_I}(\frac{\Delta V}{V} + \frac{\Delta R}{R}) \tag{38}$$

Combining **Equations 35, 42 and 36** yields:

$$\Delta Q = \Delta Q_{sen} + \frac{r_q}{r_I}\frac{V}{R}(\frac{\Delta V}{V} + \frac{\Delta R}{R}) \tag{39}$$

The uncertainty in voltages read by the data acquisition system was $\Delta V = \pm 1.790mV$. The resistance used to convert the voltage sensors to current sensors was a 500Ω resistor with an error of $\Delta R = \pm 0.5\Omega$.

Equation 39 will be used to find the error in measurements of temperature and pressure. The temperature sensors had a range of $0 - 150°C$ (so $r_T = 150°C$) with an error of $\Delta T_{sen} = \pm 0.8°C$; the error in the temperature measurements was given by:

$$\Delta T = \Delta T_{sen} + \frac{r_T}{r_I}\frac{V}{R}(\frac{\Delta V}{V} + \frac{\Delta R}{R}) \tag{40}$$

As in Section 1.1, the inlet and plenum conditions are given the subscripts 1, and

3 respectively. The error of the pressure transducers was ±0.15% of full range so $\Delta P_{1sen} = 60Pa$. The inlet pressure sensor was an $80000 - 120000Pa$ absolute pressure sensor, so $r_{P1} = 40000Pa$.

$$\Delta P_1 = \Delta P_{1sen} + \frac{r_{P1}}{r_I}\frac{V}{R}(\frac{\Delta V}{V} + \frac{\Delta R}{R}) \tag{41}$$

The plenum pressure was a $0 - 100000Pa$ gauge sensor, so $r_{P3} = 100000Pa$. Since an absolute pressure is required, the pressure indicated by this sensor must be added to the atmospheric pressure. The error in the atmospheric pressure must be added to the error in the gauge pressure to find the error in the absolute plenum pressure.

The inlet pressure sensor was used to measure atmospheric pressure before the tests began. Since the atmospheric pressure does not change greatly the error in atmospheric pressure can be calculated directly. The atmospheric pressure, P_{atm} was taken to be $101300Pa$, giving an error of $\Delta P_{atm} = 100Pa$.

The error in the absolute plenum pressure was

$$\Delta P_3 = \Delta P_{atm} + \Delta P_{3sen} + \frac{r_{P3}}{r_I}\frac{V}{R}(\frac{\Delta V}{V} + \frac{\Delta R}{R}) \tag{42}$$

3.4.1 Mass Flow Rate Calculation

The flow meter measured volumetric flow rate, and was fitted with static pressure and temperature transducers in order to convert to mass flow rate using the following equation:

$$\dot{m} = \frac{P}{RT}\dot{Q} \tag{43}$$

The temperature and pressure sensors were also $4 - 20mA$ sensors, and were connected to a flow computer. The flow computer had dedicated current sensors capable of measuring to within $\pm 9.6\mu A$. In this case the error in current is known and does not have to be calculated from errors in voltage and resistance as before. Therefore the error in each quantity is given.

$$\Delta\dot{Q} = \frac{r_Q}{r_I}\Delta I + \Delta\dot{Q}_{sen} \tag{44}$$

$$\Delta P = \frac{r_p}{r_I}\Delta I + \Delta P_{sen} \tag{45}$$

$$\Delta T = \frac{r_T}{r_I}\Delta I + \Delta T_{sen} \tag{46}$$

The overall error is given by:

$$\frac{\Delta\dot{m}}{\dot{m}} = \frac{\Delta\dot{Q}}{\dot{Q}} + \frac{\Delta P}{P} + \frac{\Delta T}{T} \tag{47}$$

The error in volumetric flow rate was 0.5% of the measured flow rate. The pressure sensor was a $0 - 10bar$ absolute sensor with an error of 0.05% of full scale.

3.4.2 Pressure Ratio Calculation

The pressure ratio is given by

$$R_p = \frac{P_1}{P_3} \tag{48}$$

The error is given by

$$\Delta R_p = \left(\frac{\Delta P_1}{P_1} + \frac{\Delta P_3}{P_3}\right) R_p \tag{49}$$

3.4.3 Error in Measuring Static Conditions

The inlet consists of a 100mm pipe. At the maximum flow rate of 115g/s, assuming a top hat velocity profile, the speed is 12m/s and the Mach number is 0.03. If the inlet total temperature is 300K and the total pressure is $101300Pa$, then the static temperature and pressure will differ from the total temperature and pressure by $0.07°C$ and $85Pa$. This difference will be neglected and the measured inlet pressure and temperature will be considered total pressure and temperature.

In order to measure total temperature at the compressor exit, the preferred method is to allow the compressor to exhaust into a large insulated plenum, through an insulated duct. The flow would be straightened by means of a honeycomb mesh, and when its speed was very low, a measurement of total temperature would be taken. However, this was not possible due to practical constraints of cost and space, therefore a correction must be made to account for this.

Then minimum total temperature is given by the measured value. The maximum value is given by assuming a uniform velocity profile at the diffuser exit with a 45 degree swirl component. The diffuser exit consists of four rectangular cross section ducts $28.3mm \times 9mm$. The maximum value for total temperature is given by:

$$T_{03max} = T_3 \left(1 + \left(\frac{\gamma - 1}{2} \right) M_3^2 \right) \tag{50}$$

Where the Mach number is calculated by

$$M_3 = \frac{C_3}{\sqrt{\gamma R T_3}} \tag{51}$$

The speed at exit is calculated by

$$C_3 = \frac{R T_3 \dot{m}}{P_3 A_3} \times 1.41 \tag{52}$$

Where A_3 is the combined cross sectional area of the four passages. The factor of 1.41 is a consequence of the assumption that the air leaves the duct at up to 45 degrees to the centerline due to the swirl component. The maximum Mach number varied between 0.09 and 0.37. The error in exit temperature is therefore adjusted to reflect this uncertainty and the measurement uncertainty. ΔT_3 represents the uncertainty in measuring T_3.

$$T_{03} = (T_{min} + T_{max})/2 \tag{53}$$

The uncertainty was calculated using

$$\Delta T_{03} = (T_{03max} - T_{03min} + 2\Delta T_3)/2 \tag{54}$$

Typical values of the quantities and errors are given in **Table 9**.

Table 9: Comparison of Meshes for Frozen Rotor simulation

Quantity	Typical Value	Error
Inlet Total Pressure	$100000Pa$	$100Pa$
Inlet Total Temperature	$20°C$	$0.9°C$
Plenum Static Pressure	140000	$140Pa$
Plenum Total Temperature	$70°C$	$3.4°C$

3.4.4 Efficiency Calculation

The calculation of the efficiency requires the total temperature and pressure at inlet, and the total temperature at the compressor exit. Since the total to static pressure ratio is used, the static pressure is measured directly at exit.

In this analysis, air is assumed to act as a ideal gas. The isentropic efficiency of a compressor is the ratio of the power (**Equation 55**).

$$\eta = \frac{\dot{W}_s}{\dot{W}} \tag{55}$$

For an ideal gas, the enthalpy change of the gas can be calculated from its change in total temperature (**Equation 56**).

$$\Delta h = C_p \Delta T_0 \tag{56}$$

Therefore the power of the compressor can be calculated (**Equation 57**).

$$\dot{W} = \dot{m} C_p \Delta T_0 \tag{57}$$

The ideal power is calculated from the pressure ratio, which is calculated from measurements of inlet end exit pressure using **Equation 58**.

$$R_p = \frac{P_3}{P_1} \tag{58}$$

Equation 59 Describes an isentropic, adiabatic change in state for an ideal gas between states a and b.

$$\left(\frac{P_a}{P_b}\right)^{\frac{\gamma-1}{\gamma}} = \frac{T_a}{T_b} \tag{59}$$

Using the definition of pressure ratio, **Equation 58**, and **Equation 57**, this can be rearranged to calculate the ideal power, given the inlet temperature, pressure ratio, and mass flow rate. (**Equation 60**).

$$\dot{W}_s = \dot{m} C_p T_{01} (R_p^{\frac{\gamma-1}{\gamma}} - 1) \tag{60}$$

For a well insulated compressor the power can be calculated from the change in the total temperature between the inlet and exit air and the flow rate using **Equation 57**. However, in the real compressor, the actual power is given by **Equation 61** where H is the heat loss.

$$\dot{W} = \dot{m}C_p(T_{03} - T_{01}) + H \tag{61}$$

The efficiency was calculated using **Equation 62**, derived by substituting **Equation** (60) and **Equation 61** into **Equation** (55).

$$\eta = \frac{T_{01}(R_p^k - 1)}{T_{03} - T_{01} + \frac{H}{\dot{m}C_p}} \tag{62}$$

Where $k = (\gamma - 1)/\gamma$.

The error associated with each parameter is calculated by taking partial derivatives. Taking each partial derivative in turn:

$$\frac{\partial\eta}{\partial T_i} = \frac{(T_o + \frac{H}{\dot{m}})(R_p^k - 1)}{(T_o - T_i + \frac{H}{\dot{m}C_p})^2} \tag{63}$$

$$\frac{\partial\eta}{\partial T_o} = -\frac{T_i R_p^k - T_i}{(T_o - T_i + \frac{H}{\dot{m}C_p})^2} \tag{64}$$

$$\frac{\partial\eta}{\partial r} = \frac{T_i k R_p^{k-1}}{T_o - T_i + \frac{H}{\dot{m}C_p}} \tag{65}$$

$$\frac{\partial\eta}{\partial H} = -\frac{T_i R_p^k - T_i}{\dot{m}C_p(T_o - T_i + \frac{H}{\dot{m}C_p})^2} \tag{66}$$

$$\frac{\partial\eta}{\partial\dot{m}} = \frac{H(T_i R_p^k - T_i)}{\dot{m}^2 C_p(T_o - T_i + \frac{H}{\dot{m}C_p})^2} \tag{67}$$

The total error in efficiency will be:

$$\Delta\eta = \left|\frac{\partial\eta}{\partial T_i}\Delta T_i\right| + \left|\frac{\partial\eta}{\partial T_o}\Delta T_o\right| + \left|\frac{\partial\eta}{\partial R_p}\Delta R_p\right| + \left|\frac{\partial\eta}{\partial H}\Delta H\right| + \left|\frac{\partial\eta}{\partial \dot{m}}\Delta\dot{m}\right| \qquad (68)$$

Errors for mass flow rate, pressure ratio and efficiency are given in Section 3.7.

3.4.5 Referred Quantities

The results are referred to the condition of 300K and 101300Pa. The referred quantities are calculated using **Equations 69 and 70**. The maximum pressure ratio was 1.52 and this was achieved at an efficiency of 50% and a mass flow rate of $78.5gs^{-1}$. This is done to take account of variations in inlet conditions [2].

$$\dot{m}_r = \dot{m}\frac{P_{ref}}{P_1}\sqrt{\frac{T_1}{T_{ref}}} \qquad (69)$$

$$\dot{\omega}_r = \omega\sqrt{\frac{T_{ref}}{T_1}} \qquad (70)$$

3.5 Results

3.6 Torque Measurement

The data from the torque meter was discredited beyond question when the torque meter read a much lower power input than the energy balance. There were no detectable systematic errors as the data was randomly spread over a range that increased with speed.

3.7 Energy Balance

Figure 31, the compressor performance map was produced from the data of **Table 10**, which also shows the errors in these quantities.

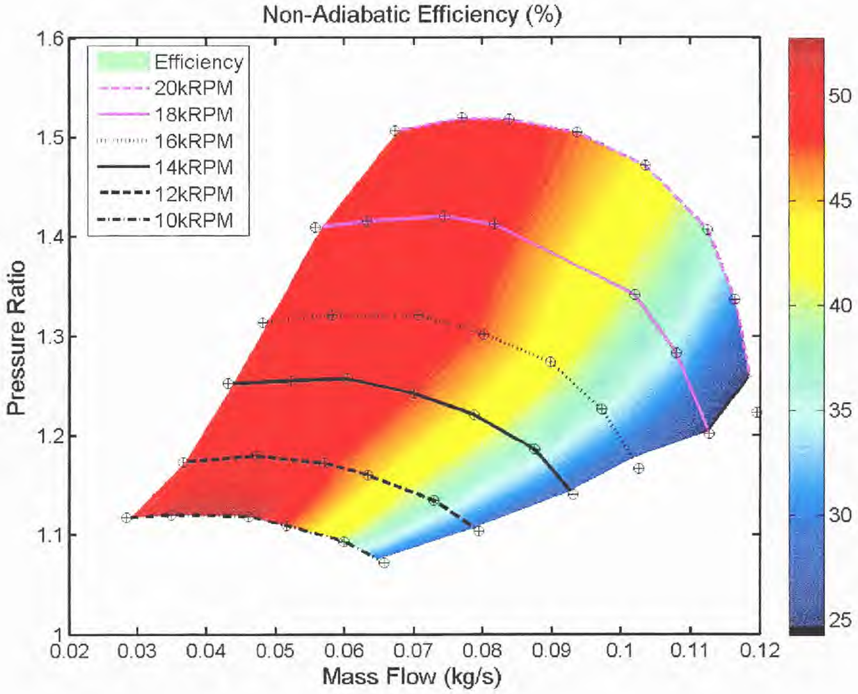

Figure 31: Performance map

Table 10: Experimental Results

Speed(ω_r)	(%error)	$\dot{m}_r$	(%error)	R_p	(%error)	η(%)	error(% points)
9960	0.6	28	1.3	1.12	0.38	50	8.4
9950	0.6	35	1.3	1.12	0.38	52	9.1
10000	0.6	46	1.3	1.12	0.39	53	10.0
9900	0.6	60	1.3	1.09	0.40	40	8.8
9920	0.6	66	1.3	1.07	0.40	27	6.2
12000	0.5	37	1.3	1.17	0.38	48	6.0
12000	0.5	47	1.3	1.18	0.38	50	6.5
11900	0.5	57	1.3	1.17	0.38	48	6.7
11900	0.5	63	1.3	1.16	0.38	45	6.7
12100	0.5	73	1.3	1.13	0.39	38	6.4
12100	0.5	79	1.3	1.10	0.40	28	5.1
14400	0.4	43	1.3	1.25	0.37	49	4.7
14300	0.4	52	1.3	1.25	0.37	50	5.0
14400	0.4	60	1.3	1.26	0.37	50	5.2
14300	0.4	70	1.3	1.24	0.37	48	5.4
14400	0.4	79	1.3	1.22	0.38	44	5.4
14400	0.4	88	1.3	1.19	0.39	37	5.1
14400	0.4	93	1.3	1.14	0.40	26	4.1
16000	0.4	48	1.3	1.31	0.36	48	4.0
16000	0.4	58	1.3	1.32	0.36	50	4.3
16000	0.4	71	1.3	1.32	0.36	50	4.6
16000	0.4	80	1.3	1.30	0.37	47	4.7
16000	0.4	90	1.3	1.27	0.37	42	4.7
16000	0.4	97	1.3	1.23	0.39	36	4.4
16000	0.4	103	1.3	1.17	0.40	26	3.6
18100	0.3	56	1.3	1.41	0.35	49	3.4
18100	0.3	63	1.3	1.42	0.35	49	3.5
18100	0.3	75	1.3	1.42	0.35	50	3.8
18000	0.3	82	1.3	1.41	0.36	49	3.9
17900	0.3	102	1.3	1.34	0.37	40	3.9
17900	0.3	108	1.3	1.28	0.38	34	3.7
18100	0.3	113	1.3	1.20	0.40	24	3.0
20000	0.3	67	1.3	1.51	0.34	48	3.0
20000	0.3	77	1.3	1.52	0.34	49	3.1
19800	0.3	84	1.3	1.52	0.35	48	3.2
19900	0.3	94	1.3	1.50	0.35	47	3.4
20600	0.3	104	1.3	1.47	0.36	44	3.4
19800	0.3	113	1.3	1.41	0.37	38	3.3
20100	0.3	116	1.3	1.34	0.38	31	3.0
19800	0.3	120	1.3	1.22	0.40	21	2.4

3.8 Discussion

3.8.1 Torque meter

The torque meter was sent back to the manufacturer on several occasions. On one occasion a fault was found and repaired (a broken piezoelectric crystal), but no improvement in the meter's function was evident. The manufacturer eventually admitted that they had no facility to test the torque meter under load at high speed. The meters were tested statically for calibration, and then spun with no load to the full rated speed of $25,000rpm$ to ensure the bearings were capable for the full speed. Since the problem only occurs at speed and under load the manufacturer could not even detect the problem, and therefore could not diagnose or rectify it.

The measurement of torque at this speed is considered technically feasible and should be attempted in future with a torque meter from a different manufacturer.

3.8.2 Energy Balance

In the tests the minimum heat loss was 5% of the input shaft power and the maximum was 15%. At the maximum pressure ratio the heat loss was 6.5% of the shaft power. Therefore the efficiency calculated is not the isentropic efficiency. It will be referred to as the non-adiabatic efficiency, based on the work of Shaaban and Seume [25].

The testing standard, ASME PTC 10-1997, for compressors was used to assess the experiments. The tests of efficiency that have been performed do not meet all of the criteria of the testing standard, and this is reflected in the large error bands.

A summary of the requirements follows:

- "that total heat loss due to radiation and convection should be <5% of total shaft power"

This criterion has been dealt with by refereing to the calculated efficiency as non-adiabatic.

- "that the combined accuracy of the measurement of temperature rise should be <1%."

  The error in temperature measurement was less than 4% for speeds above 14000rpm. Below 14000rpm, the maximum error is 8% of the temperature difference. This is reflected in the errors in efficiency quoted.

- "that great care should be taken if the temperature rise across a stage is <50°F (approximately 31° C)."

  At speeds above 12000rpm the temperature rise was above this limit. The minimum temperature rise is $15°C$.

- "that fluctuations in the temperature distribution at either the inlet or exit measuring stations should be <2% of the temperature rise across the stage."

- "that the compressor must reach thermal equilibrium, demonstrated by six or more readings uniformly timed over a period of no less than 10 minutes, during which the temperature rise drift does not exceed 5%."

  Temperature readings were allowed to stabilize to within 0.5 degrees over a 10 minute period. Six readings were recorded and averaged over this time. This fulfills the criteria for all data points. It fulfills the previous criteria for all speeds of 12000rpm and above.

This discussion shows why torque measurements would have been preferred. However the data produced gives an indication of the compressor's performance within the error bands quoted. For mature designs it is necessary to know the efficiencies to higher precision and this accounts for the high accuracies required by the test code.

3.9 Conclusion

The current design has achieved a pressure ratio of 1.52 at an efficiency of 49% ± 3.1 percentage points. The measurement of torque should be pursued because it is technically feasible and there are large errors in the heat balance method at low flow rates.

4 Computational Modelling

4.1 Introduction

The following section describes the computational modelling of the compressor. The governing equations for a compressible Newtonian fluid are presented and because the flows considered are turbulent, the equations are then time averaged to give the Reynolds averaged equations for the continuity of mass, momentum and enthalpy.

The Boussinesq approximation is used to model the turbulent diffusion of momentum and enthalpy via an eddy viscosity model. The turbulence model used in the simulations was the $k - \omega$ Shear Stress Transport model as implemented in CFX version 02.12.01. This model uses the $k - \epsilon$ model in regions far from the wall, and the $k - \omega$ model near the wall to calculate the eddy viscosity.

To reduce computational demands the symmetry of the rotor and diffuser was exploited, that is, three rotor blades and a single diffuser blade were included in the model with periodic boundary conditions. The compressor was modelled at its design point of $90g/s$ at $20,000rpm$. The boundary conditions were, therefore, a mass flow rate of $90g/s$, a temperature of $300K$ at inlet and a static pressure of $160000Pa$ at exit as this gave near atmospheric pressure at inlet.

A frozen rotor interface was used between the rotor and the diffuser. Four meshes of increasing resolution were analysed.

The solution was not mesh independent as there were still variations in the solution as the mesh resolution increased. The geometry is difficult to mesh effectively without a high element count. The solutions suggest that a transient solution may be required.

4.2 Fluid Model

The conservation equations for mass, momentum and energy for a compressible Newtonian fluid are written [26].

$$\frac{\partial \rho}{\partial t} + \frac{\partial}{\partial x_j}(\rho U_j) = 0 \tag{71}$$

$$\frac{\partial}{\partial t}(\rho U_i) + \frac{\partial}{\partial x_j}(\rho U_i U_j) = -\frac{\partial P}{\partial x_i} - \frac{\partial \tau_{ij}}{\partial x_j} + \rho f_i \tag{72}$$

$$\frac{\partial}{\partial t}(\rho H) + \frac{\partial}{\partial x_j}(\rho U_j H) = \frac{\partial P}{\partial t} - \frac{\partial}{\partial x_j}(U_i \tau_{ij} + Q_j) + \rho U_i f_i \tag{73}$$

Where τ_{ij} is the viscous stress tensor and Q_j represents heat conduction (Fourier's law). The equation of state is also required to close the set of equations. In this study the working fluid is air which is treated as a perfect gas.

$$Pv = RT \tag{74}$$

4.2.1 Reynolds Averaging

Equations 71,72 and 73 represent the conservation of mass, momentum and energy in any Newtonian fluid. Most flows of engineering interest are turbulent - that is the flow includes complex chaotic turbulent eddies that cannot be resolved with present computing resources. In an attempt to provide a more manageable description of the turbulent flow, each flow variable is assumed to have a time averaged component superposed with a fluctuating turbulent component, for example:

$$U_i = \overline{U_i} + u_i' \tag{75}$$

$$P = \overline{P} + p' \tag{76}$$

$$H = \overline{H} + h' \tag{77}$$

The governing equations are written with these terms and then averaged over time resulting in transport equations containing, in addition to the time averaged quantities, averaged products of turbulent velocity components. The $\rho\overline{\mathbf{u}'u_i'}$ terms are known as Reynolds stresses and represent unknown quantities that need to be specified to close the equation set. Eddy viscosity models of turbulence are based on the assumption that the turbulence has a similar effect to a molecular diffusion term. In the momentum equation this means the Reynolds stresses are modelled via a turbulent viscosity and in the energy equation via a turbulent diffusivity. This is plausible since turbulence is a mixing process which causes momentum and thermal energy to diffuse more rapidly than if molecular processes only were present. The Reynolds stresses are specified in terms of the Boussinesq approximation:

$$\rho\overline{u_i'u_j'} = \frac{2}{3}\rho\delta_{ij}k - \mu_t\left(\frac{\partial\overline{U_i}}{\partial x_j} + \frac{\partial\overline{U_j}}{\partial x_i}\right) + \frac{2}{3}\delta_{ij}\mu_t\frac{\partial\overline{U_l}}{\partial x_l} \tag{78}$$

Where δ_{ij} is the Kronecker delta, k is the turbulent kinetic energy, and μ_t is the eddy viscosity. Substituting the Boussinesq approximation (**Equation 78**) into the Reynolds averaged continuity equations results in:

$$\frac{\partial\rho}{\partial t} + \frac{\partial}{\partial x_j}(\rho\overline{U_j}) = 0 \tag{79}$$

$$\frac{\partial}{\partial t}\left(\rho\overline{U_i}\right)+\frac{\partial}{\partial x_j}\left(\rho\overline{U_iU_j}\right)=-\frac{\partial P^*}{\partial x_i}+f_i+\frac{\partial}{\partial x_j}\left\{\mu_{eff}\left(\frac{\partial\overline{U_i}}{\partial x_j}+\frac{\partial\overline{U_j}}{\partial x_i}\right)-\frac{2}{3}\mu_{eff}\frac{\partial\overline{U_l}}{\partial x_l}\right\} \tag{80}$$

$$\mu_{eff}=\mu+\mu_t \tag{81}$$

$$\begin{aligned}\frac{\partial}{\partial t}(\rho H)-\frac{\partial P}{\partial t}+\frac{\partial}{\partial x_j}(\rho\overline{U_i}H)&=\frac{\partial}{\partial x_j}\left(\lambda\frac{\partial T}{\partial x_j}+\frac{\mu_t}{Pr_t}\frac{\partial h}{\partial x_j}\right)+S_E\\&+\frac{\partial}{\partial x_j}\left\{\overline{U_i}\left[\mu_{eff}\left(\frac{\partial\overline{U_i}}{\partial x_j}+\frac{\partial\overline{U_j}}{\partial x_i}\right)-\frac{2}{3}\mu_{eff}\frac{\partial\overline{U_l}}{\partial x_l}\delta_{ij}\right]+\mu\frac{\partial k}{\partial x_j}\right\}\end{aligned} \tag{82}$$

The governing equations are similar to **Equation 72 and 73** except that the viscosity is now the sum of the molecular and the turbulent viscosities and the diffusivity is also the sum of modelled molecular and turbulent diffusivities.

Numerous eddy viscosity models exist which specify the eddy viscosity algebraically or via the use of one or more transport equations for turbulence properties; this work uses the $k-\omega$ Shear Stress Transport (SST) option in CFX 02.12.01.

The $k-\omega$ SST model uses the $k-\omega$ model of Wilcox [27] in the region near solid boundaries and the $k-\epsilon$ model of Launder and Sharma [28] in the free stream.

The $k-\omega$ model is similar to its predecessor, the $k-\epsilon$ model. In both models, k represents the turbulent kinetic energy which is modelled by an additional transport equation derived from the momentum equations i.e.

$$\frac{\partial(\rho k)}{\partial t}+\frac{\partial(\rho\overline{U_j}k)}{\partial x_j}=\frac{\partial}{\partial x_j}\left(\Gamma_k\frac{\partial k}{\partial x_j}\right)+P_k-\rho\epsilon \tag{83}$$

$$\Gamma_k = \mu + \frac{\mu_t}{\sigma_k} \tag{84}$$

$$P_k = \mu_t \left(\frac{\partial \overline{U_i}}{\partial x_j} + \frac{\partial \overline{U_j}}{\partial x_i} \right) \frac{\partial \overline{U_i}}{\partial x_j} - \frac{2}{3} \left(\rho k + \mu_t \frac{\partial \overline{U_l}}{\partial x_l} \right) \frac{\partial \overline{U_k}}{\partial x_k} \tag{85}$$

ϵ is the dissipation rate of turbulent kinetic energy, which is yet to be calculated. Dimensional arguments lead to the calculation of the turbulent viscosity using the following equation. C_μ is a dimensionless constant.

$$\mu_t = \rho C_\mu \frac{k^2}{\epsilon} \tag{86}$$

This only leaves the problem of describing how turbulence is dissipated. In two equation models, the dissipation is modelled in a further transport equation. The most common way is to model the parameter ϵ, the dissipation rate.

The modelled equation for dissipation rate are shown below. The coefficients are found from a broad range of empirical data such as boundary layer flow, wake flow and jet flow.

$$\frac{\partial(\rho\epsilon)}{\partial t} = \frac{\partial(\rho \overline{U_j} \epsilon)}{\partial x_j} = \frac{\partial}{\partial x_j} \left(\Gamma_\epsilon \frac{\partial \epsilon}{\partial x_j} \right) + \frac{\epsilon}{k}(c_{\epsilon 1} P_k - \rho c_{\epsilon 2} \epsilon) \tag{87}$$

$$\Gamma_\epsilon = \mu + \frac{\mu_t}{\sigma_\epsilon} \tag{88}$$

$C_\mu = 0.09$, $\sigma_\epsilon = 1.30$, $C_{1\epsilon} = 1.44$, $\sigma_k = 1.0$,$Pr_t = 0.9$ and $C_{2\epsilon} = 1.92$

This approach allows the history of the fluid to be taken into account as the turbulent properties are transported with the fluid.

The $k-\omega$ model is similar and also uses two equations to model turbulence. Instead of the dissipation rate ϵ, the dissipation rate per unit kinetic energy is modelled in a transport equation ($\omega = \epsilon/k$). The equations for k and ω are:

$$\frac{\partial(\rho k)}{\partial t} + \frac{\partial(\rho \overline{U_j} k)}{\partial x_j} = P_k - \beta^* \rho k \omega + \frac{\partial}{\partial x_j}\left[\left(\mu + \frac{\mu_t}{\sigma_k}\right)\frac{\partial k}{\partial x_j}\right] \tag{89}$$

$$\frac{\partial(\rho \omega)}{\partial t} + \frac{\partial(\rho \overline{U_j} \omega)}{\partial x_j} = \alpha \frac{\omega}{k} P_k - \beta \rho \omega^2 + \frac{\partial}{\partial x_j}\left[\left(\mu + \frac{\mu_t}{\sigma_\omega}\right)\frac{\partial \omega}{\partial x_j}\right] \tag{90}$$

$$P_k = \mu_t 2 S_{ij} \frac{\partial \overline{U_i}}{\partial x_j} \tag{91}$$

$$S_{ij} = \frac{1}{2}\left(\frac{\partial \overline{U_i}}{\partial x_j} + \frac{\partial \overline{U_j}}{\partial x_i}\right) \tag{92}$$

$\beta^* = 0.09$, $\alpha = 5/9$, $\beta = 3/40$, $\sigma_k = 2$, $\sigma_\omega = 2$

4.2.2 $k - \omega$ and $k - \epsilon$ Turbulence Models

So far, the basic forms of the $k - \epsilon$ and the $k - \omega$ turbulence models have been presented. The implementation of these turbulence models in commercially available CFD packages has required some refinement of these basic models. The work of Bardina et al [29] compares a typical implementation of the $k - \epsilon$ model (the Launder-Sharma model [28]), the standard $k - \omega$ model described by Wilcox [27] and the SST model described by Menter [30] which uses the $k - \omega$ model near the wall, and the $k - \epsilon$ model in the rest of the flow.

The Launder-Sharma model (sometimes referred to as the standard $k - \epsilon$ model) employs damping functions near the wall to correctly model the dissipation of k when k^2 is very small compared to ϵ, which occurs near the wall.

The $k - \omega$ model was developed by Wilcox [27] as an attempt to improve boundary layer modelling as damping functions are not required (unlike the $k - \epsilon$ model). However this approach does not model flow in the free stream effectively as it is sensitive to changes in free stream turbulence. Therefore Menter [30] proposed a blending function that provides a smooth transition between the $k-\omega$ model near the wall and the $k-\epsilon$ model in the rest of the flow.

Menter proposed a further enhancement to deal with boundary layer separation. In flows where an adverse pressure gradient causes the boundary layer to separate, the best agreement with experimental data is provided by assuming that the Reynolds stresses are proportional to the turbulent kinetic energy, rather than a function of velocity gradient and turbulent viscosity. In such flows the production of turbulent kinetic energy is greater than its dissipation and under these circumstances eddy viscosity models overestimate Reynolds stresses. Therefore another blending function is employed to switch from a model of shear stress based on velocity gradient to a model based on turbulent kinetic energy when production of turbulent kinetic energy exceeds dissipation rate. This is known as the Shear Stress Transport model.

Bardina et al [29] concludes that the best overall model is the SST model since the $k-\epsilon$ model did not model separated flow effectively, and the Wilcox $k-\omega$ model did not model free stream flow effectively.

4.3 The Log Law of the Wall

In most engineering situations a boundary layer on a solid surface exists and must be modelled. In modelling near wall turbulent boundary layers, the Navier-Stokes equations are solved throughout the boundary layer; this is referred to as a low Reynolds number model, or a natural boundary layer model. In such models, high near wall resolution is required. The first node from the wall must be closer than $y^+ = 2$ and at least 15 nodes are required within the boundary layer. In cases where the boundary layer cannot be resolved or where high Reynolds number turbulence models are used the near wall behavior is modelled using the log law of the wall. Experimental data for attached, turbulent, incompressible boundary layer flow on a flat plate is described by the log law **Figure 32**. The velocity profile is expressed in terms of u^+ and y^+; dimensionless forms of the velocity and the distance from the wall, defined by **Equations 93 and 94**, where τ_0 is the shear stress at the wall, u is the velocity and y is the distance from the wall.

$$u^+ = u\left(\frac{\tau_0}{\rho}\right)^{-\frac{1}{2}} \tag{93}$$

$$y^+ = \frac{y}{\nu}\left(\frac{\tau_0}{\rho}\right)^{\frac{1}{2}} \tag{94}$$

The plot is divided into three regions. The first is the laminar sub-layer where laminar shear stress dominates; in this region $u^+ = y^+$. The second is a transition between laminar sub-layer and the log law layer. The third is the log law layer in which turbulent stresses dominate and in which

$$u^+ = \frac{1}{\kappa}\ln y^+ + C \tag{95}$$

The constants κ (Von Karman's constant) and C are determined experimentally.

In cases where the near wall boundary layer cannot be resolved it is necessary that the grid line adjacent to the solid boundary is in the log law region of the log law on the wall. In these cases, y^+ should be greater than 30 and less than 200.

4.4 Discretisation

Discretisation is the conversion of the continuous differential equations into their discrete counterparts to enable a numerical solution. The upwind difference scheme was used, which is first order accurate.

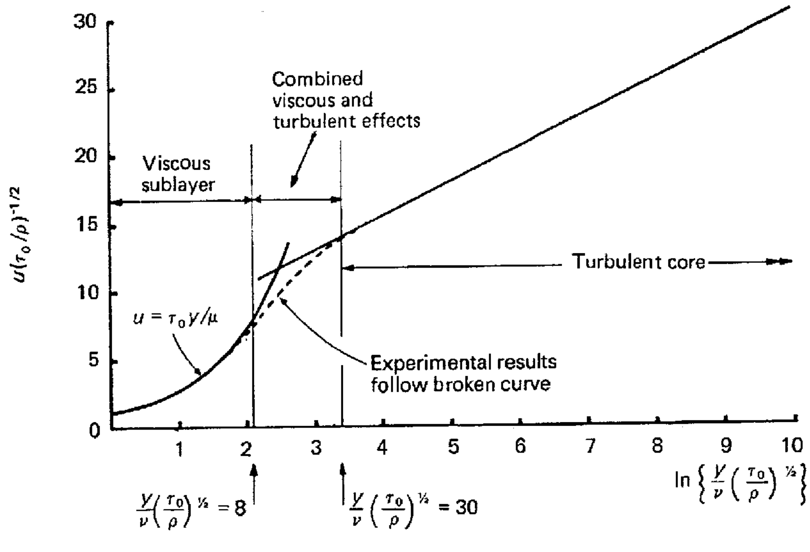

Figure 32: The log law boundary layer [31]

4.5 Mesh Generation

The compressor geometry developed in section 2 was analysed. The geometry of the compressor consists of 12 rotor blades and 4 diffuser blades. The rotational symmetry of the design means that only a single diffuser blade, and three rotor blades needed to be analysed which reduces the overall computational cost.

The geometry of a blade is specified by three data files containing, the hub, shroud and blade profiles. The hub and shroud profiles are each a single curve, defined by a set of points in x, y and z coordinates. These curves are used to generate surfaces of revolution that define the hub and shroud geometry. In the present work, the hub and shroud profiles are straight lines, which generate planes a distance of 9mm apart, except for the near the exit of the diffuser where the exit the shroud profile tapers towards the hub profile; this tapering was found to improve computational stability, and is discussed further in section 4.8.2.

The blade profile may consist of many cross sections of the blade throughout its height, again expressed as lists of points in x, y, and z coordinates to allow for blades that change cross section throughout their length, as is the case with most turbomachinery. In the present work, the blades are simple prisms, and therefore only two profiles are required which must lie on the hub and shroud surfaces.

In order to create the computational mesh, the rotor and diffuser blades were meshed separately, and then combined. The meshing was performed in Turbogrid 01.06.00, the CFX meshing application for turbomachinery. In order to define the geometry, the axis of rotation the number of blades in 360° and the hub, shroud, and blade profiles are needed.

Turbogrid works by applying mesh templates to the input geometry. The user is required to fit the template to the geometry by dragging control points to fit the template to the actual geometry.

As the control points are moved by the user the user needs to monitor three important mesh quality parameters, namely aspect ratio, skew angle and near wall resolution. The aspect ratio is the ratio of the longest side of the cell to the shortest; it should be less than 100, and preferably under 10. In areas of the mesh where each adjacent cell is larger than the last, the expansion ratio, that is, the ratio of the length of one cell divided by the length of the next should be less than 1.3. The angle between adjacent cell faces is known as the skew angle and the minimum should be 20 degrees. The requirement that y^+ should be less than 100 has already been discussed. These requirements are based on advice from the CFX documentation [26], and papers which discuss past work [32].

In addition to the mesh quality the overall size of the computational mesh is limited by the computational resources available and the need to resolve the important features of the flow correctly.

If the solution is a true representation of the flow then it will not be affected by further refinements of the mesh. It is necessary to establish mesh independence by running the same geometry and boundary conditions with meshes of different resolution.

in order to minimise skew angles. The control points are linked by lines which indicate the skeleton of the mesh. The "Generic - Single Block Grid" (**Figure 33**) was used and **Figure 34** shows this template applied to the highly forward swept rotor blade. The yellow control points have a single degree of freedom since they are either constrained to be on the blade surface, or at a radius fixed by the inlet or outlet radius. The green control points have two degrees of freedom.

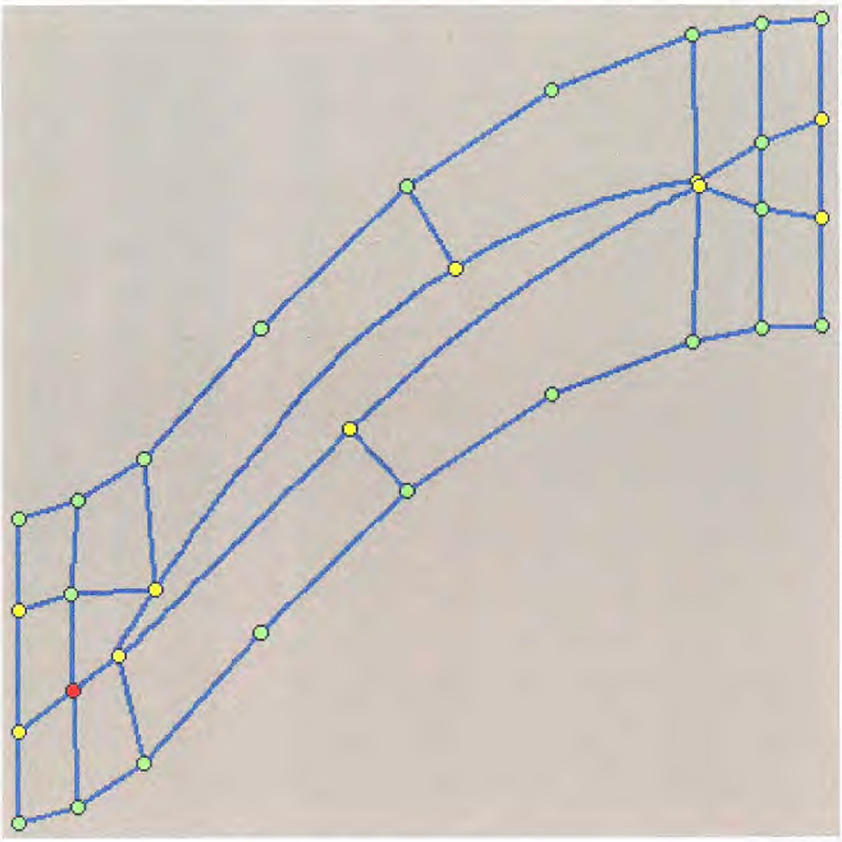

Figure 33: Generic Single Block Grid

Figure 34: Generic Single Block Grid Applied to Rotor Geometry

The mesh of the volume surrounding the blade must have two faces that are rotationally symmetrical about the axis of rotation of the compressor and have an angular displacement of the blade pitch angle. This means that multiple blades can be joined together, and periodic boundary conditions can be applied to a single blade or a group of blades.

For the generic single block grid, the control points on the periodic faces are constrained to be in the same place when rotated through the blade angle, ensuring that the shape and also the mesh on the periodic faces are identical. The grey lines in **Figure 34** show the topology of the blade and control points duplicated on each side of the blade, indicating how it will be connected to neighboring blades.

The user can set the number of mesh cells along each line, and their expansion ratio. In order to control the expansion ratio, a line of the mesh can be divided into as many sections as required and each section given a different expansion ratio. The line is divided by specifying a percentage of its length that should have a specified expansion ratio. Therefore if a line needs an expansion ratio of 1.2 for half of its length and no expansion of the cells for the other half, this is specified by entering the distribution for that line in Turbogrid as:

50@1.2 50@1

If the refined mesh is required at the other end of the line, this is specified by setting the distribution to:

50@1 50@0.833

In the second case, each cell is smaller than the previous one, so the reciprocal of the original expansion ratio should be used.

Meshes of differing mesh density were created in the course of the project. In each case the number of cells along each line, and the expansion ratios for each line were set manually.

Four mesh assemblies of increasing mesh density were created to investigate the mesh density on the solution. Different numbers of elements were specified on each of the lines, although the control points were not moved. In addition, different expansion ratios were set at the ends of the lines in order to control the near wall resolution. The gross properties of meshes A, B, C, and D are shown in **Table 11**.

Table 11: Comparison of Meshes A, B, C and D

Mesh	Rotor elements	Diffuser elements	Max. Aspect ratio (Diffuser/Rotor)	Max Bias ratio (Diffuser/Rotor)
A	3968	7056	120/300	6/4
B	19080	41775	100/90	4/3
C	39482	100248	85/80	2.5/3
D	67988	194760	100/65	1.3/1.3

In the table, mesh parameters for the diffuser and then the rotor meshes are shown separated by a forward slash. In the mesh assembly there are three rotor blade meshes. Mesh C is shown in **Figure 35** to illustrate how the topology is applied to the real geometry.

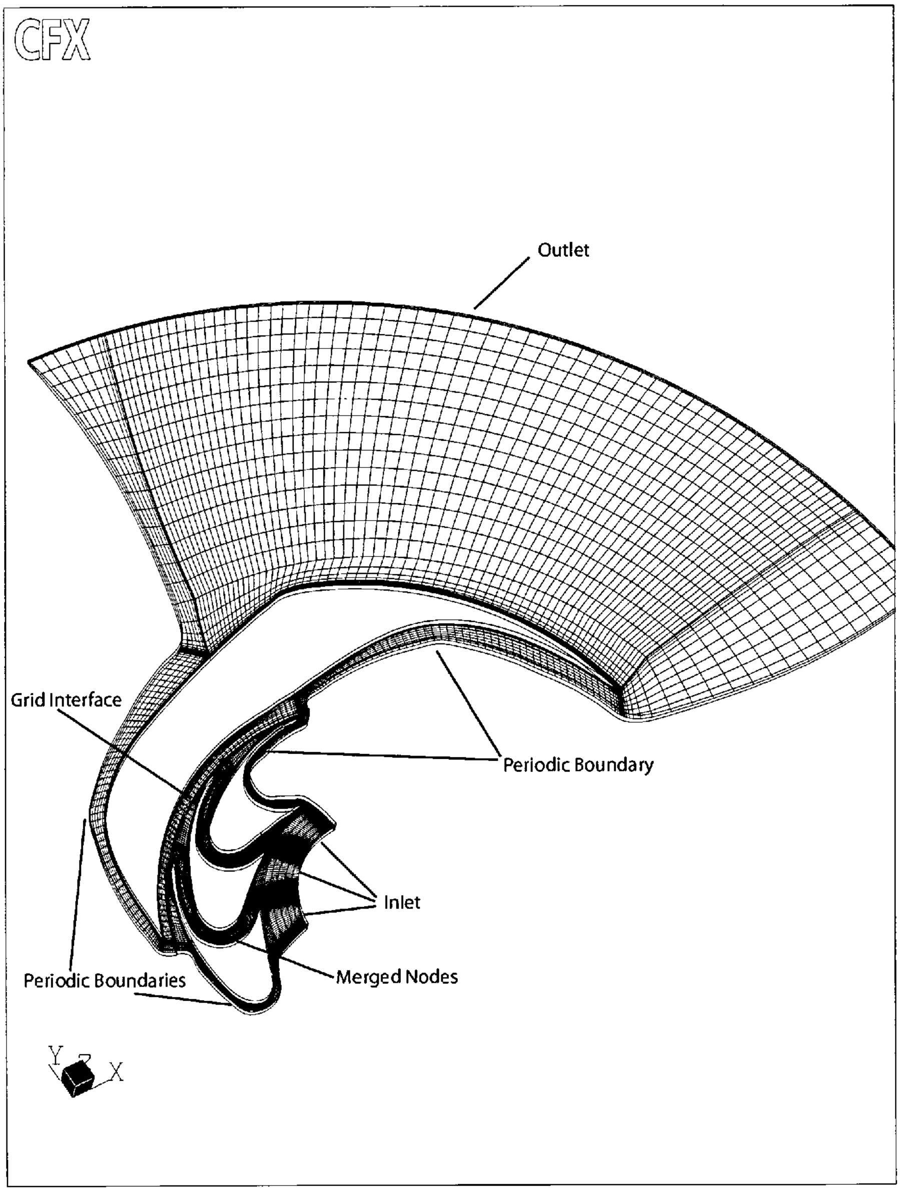

Figure 35: Computational Domain

4.6 Boundary Conditions

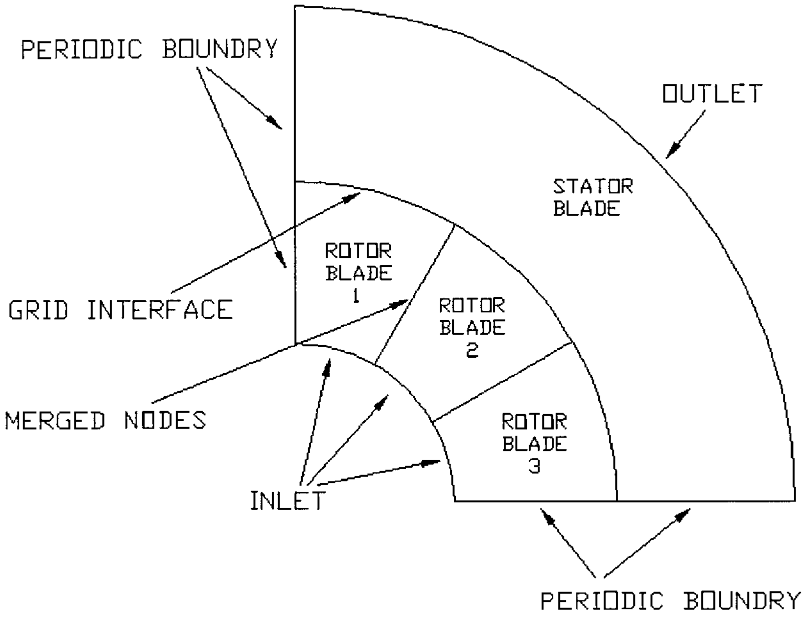

Figure 36: Topology of Compressor Mesh Assembly

The topology of the compressor assembly is indicated by **Figure 36**. The three rotor blades were generated by creating three copies of the rotor blade mesh, such that each copy was rotated 30 degrees from the last. The nodes on the periodic faces of the rotor matched exactly, so the three rotor blade meshes were simply joined together as if they were a single block, by merging the coincident nodes.

The rotor and diffuser were modelled as separate fluid domains with a grid interface between them. The rotor domain was rotating at the rotational speed of the compressor, and the diffuser domain was stationary. The fluid in the rotor domain had body forces applied to it to account for the centrifugal and coriolis forces in the rotating frame of reference.

The rotor and diffuser domains had a grid interface between them, in order to deal with the change in frame of reference. This was a "frozen rotor" interface, meaning that there was no averaging across the interface, and no sliding at the interface (no relative movement of the meshes).

4.6.1 Walls

All the surfaces that were not inlets or outlets were set to be walls. The surfaces were found to be hydraulically smooth in the large scale rig. This was after an examination of BS1134:Part 2 which gives roughness values produced by common machining processes. The values are given in terms of R_a which is defined as "the arithmetic average value of the departure of the profile above and below the reference line throughout the prescribed sample length". The Moody diagram uses roughness values based on different grades of sand glued to the wetted wall so these values are not exactly analogous, although this value can be used as high precision is not required. The maximum common roughness is $6.3\mu m$ for turning and milling. The finish on the diffuser was excellent and so this is probably an overestimation. In a $9mm$ high passage, the relative roughness is 7×10^{-4}. The maximum gas speed is $300ms^{-1}$ so the maximum Reynolds number is 1.8×10^5. An examination of the Moody diagram [33] shows that the surface can be considered hydraulically smooth. As an energy boundary condition is also required, the walls were specified as adiabatic.

4.6.2 Inlet

The inlet was set to a mass flow boundary condition. The mass flow required is a quarter of $90gs^{-1}$ since only a quarter of the compressor is analysed. A top-hat inlet profile was used at the inlet, and the gas entered radially in the absolute frame. The inlet temperature was set to be 300K.

Boundary conditions for turbulence are in the form of the turbulent viscosity ratio and the turbulence intensity. The turbulent intensity is linked to the turbulent kinetic energy and the free stream velocity as defined by **Equation 96**. At the inlet, the turbulence intensity T_i was set to 0.05.

$$T_i = \frac{(\frac{2}{3}k)^{\frac{1}{2}}}{U} \tag{96}$$

k was calculated from the turbulent intensity and the inlet velocity.

$$k = \frac{2}{3}U^2 T_i^2 \tag{97}$$

ϵ was calculated from k and the characteristic length. The characteristic length l is half the passage height, since this is a representative size for the largest eddies.

$$\epsilon = \frac{k^{\frac{2}{3}}}{l} \tag{98}$$

The turbulent viscosity was calculated from values of k and ϵ.

$$\mu_t = \rho C_\mu \frac{k^2}{\epsilon} \tag{99}$$

Using values of $U = 30ms^{-1}$, $l = 4.5mm$, $\mu = 1.8 \times 10^{-5}$ and $C_\mu = 0.09$ the ratio of turbulent viscosity to molecular viscosity was found to be 33.

In specifying the inlet boundary conditions, the turbulent intensity was set to 5% and the viscosity ratio was set to 10, these values being representative of the order of magnitude of the inlet turbulence conditions.

4.6.3 Exit boundary condition

The pressure ratio of the compressor was known to be close to 1.6 from previous simulations. A static pressure boundary condition of $160000Pa$ was applied to the exit of the diffuser domain to obtain near atmospheric inlet conditions.

4.7 Results

The results of the frozen rotor simulations are presented in **Table 12**. The run time is the actual time that CFX took to converge when running on an Athlon 3200 PC, with 2 gigabytes of 400MHz DDR RAM.

Table 12: Comparison of Meshes for Frozen Rotor simulation

Mesh	Converged	Run Time	Pressure Ratio	Efficiency	y^+ Max	y^+ Bulk
A	Yes	1h 43min	1.52	57	800	800
B	Yes	3h 11min	1.57	64	100	250
C	Yes	8h 13min	1.53	59	100	400
D	No	-	-	-	-	-

In order to calculate the efficiency and pressure ratio, inlet and exit conditions were required. The mass averaged total pressure was calculated at the inlet of the rotor, and the area averaged static pressure was calculated at the outlet of the diffuser passage. The total to static pressure ratio was calculated by dividing the average outlet pressure by the average inlet pressure.

The efficiency was calculated by comparing the work for an ideal compressor of the same pressure ratio with the actual work calculated from the temperature rise (total temperature was used at the inlet and the exit). **Equation 100** was used; R_p is the pressure ratio.

$$\eta = \frac{T_{01} R_p^{\frac{\gamma}{\gamma-1}} - T_{01}}{T_{03} - T_{01}} \tag{100}$$

The maximum value of y^+ was seen at the leading edge of the diffuser and the maximum value of y^+ in the rest of the domain is also given as the "bulk" value.

4.8 Discussion

The values of pressure ratio and efficiency in **Table 12** vary between different meshes. The efficiency for meshes A and B differs by 7 percentage points, and the efficiency for meshes B and C differs by 5 percentage points. There is an increase of efficiency between meshes A and B and a decrease between meshes B and C. The pressure ratio follows a similar trend; it increases from 1.52 for mesh A to 1.57 for Mesh B and then decreases to 1.53 for mesh C. The increase in cell count between meshes A and B is a factor of approximately 5, whereas the increase in cell count between meshes B and C is approximately 2, and therefore a smaller difference between meshes B and C would be expected than the difference between meshes A and B (**Table 11**). The significant differences between the results means that the solution should not be considered mesh independent.

4.8.1 Mesh Quality

This geometry has inherent meshing difficulties. The long thin passages give rise to long thin cells. The high speed flow in the scroll part of the diffuser means that the boundary layer is extremely thin and the position of $y^+ = 100$ is very close to the wall. As stated in section 4.3, the first node must be within $y^+ < 100$. This means that the long thin cells are made even thinner as the mesh is refined in a direction perpendicular to the wall. Additionally, a smooth growth of the cells is required in this direction causing a high cell count. Further refinement in order to make the cells shorter parallel to the wall is undesirable as the cell count is already high so a high aspect ratio is unavoidable. This aspect ratio is seen not only near the wall, but in the

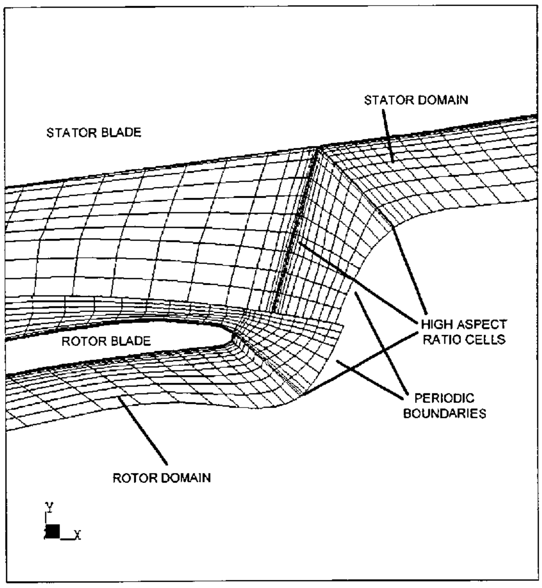

Figure 37: Mesh C Detail

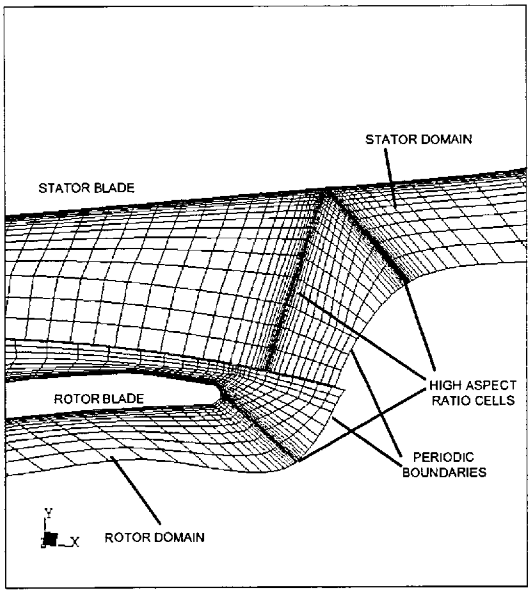

Figure 38: Mesh D Detail

main part of the passage as shown in **Figure 38**.

Mesh D (**Figure 38**), where the grid biasing ratio and the cell size near the wall fulfill the relevant criteria, failed to converge i.e. the residuals did not reach their target value. Mesh C (**Figure 37**) is the most refined mesh that converged.

4.8.2 Exit Geometry

Problems at the exit of the computational domain were experienced. The gas velocity at the exit of the control volume was low, and even small disturbances in the flow cause a tendency for flow to re-enter the stationary domain at its outlet. The CFX solver fixes this problem by placing walls at the exit at regions where the flow tends to flow into the outlet. The problem can be greatly alleviated by reducing the axial height near the exit in order to accelerate the gas out of the computational volume. The actual plenum was not modelled, so the exit region, walls and pinch are not physical.

This geometry was not identical to the test and this is a shortcoming of the model. In the calculation of exit conditions a region at the exit of the diffuser passage was used. Newer versions of CFX allow volutes and plenums to be added, and this should be used in future work in order to create an accurate version of the geometry that was tested.

4.8.3 Mesh Independence

Figure 39, 40 and 41 show the velocity vectors for the first passage for each of the meshes. These and all the plots in this section show velocity vectors at a plane mid way between the hub and shroud planes. The arrows are a constant size in order to improve clarity; the colour indicates the velocity magnitude. The velocity vectors of the rotor are in the rotor's frame of reference, which explains the apparent step change in velocity between the rotor and diffuser.

For this passage, much of the flow is reversed; it is flowing from "C" to "A" rather than "A" to "C" as intended. The blue vectors indicate that this flow is slow moving. The separation at "A" appears in all three meshes. In Mesh C at "B" there is a change in the velocity direction. Since the flow in this region is slow, this represents a relatively small change in the velocity.

At the blade trailing edge at "C" there is a very small swirling flow structure which is progressively more resolved as the resolution increases from Mesh A (**Figure 39**) to Mesh C (**Figure 41**). Even in Mesh C it is unlikely that this feature is well resolved as the velocity changes direction within a few cells.

At "D" in the diffuser, slow moving flow is more evident as the Mesh resolution increases. No slow moving region is shown in Mesh A, Mesh B (**Figure 40**) shows some slow moving flow indicated by light blue vectors, and Mesh C shows very slow moving flow indicated by dark blue vectors.

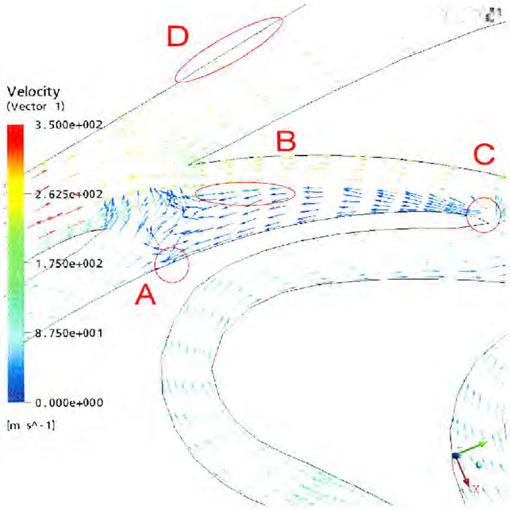

Figure 39: Mesh A - Velocity Vectors First Passage

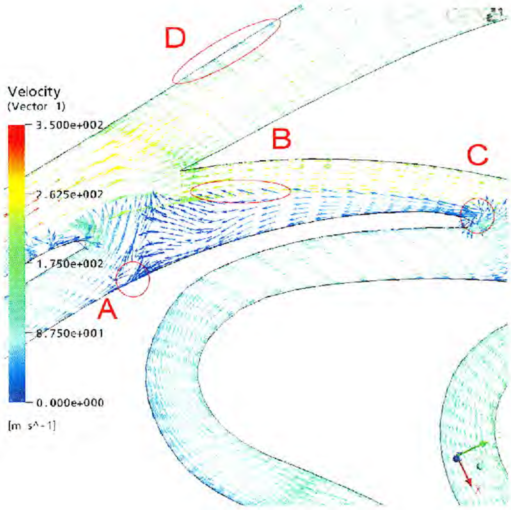

Figure 40: Mesh B - Velocity Vectors First Passage

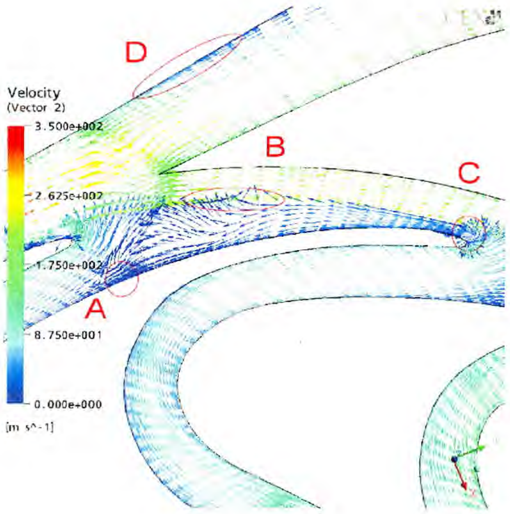

Figure 41: Mesh C - Velocity Vectors First Passage

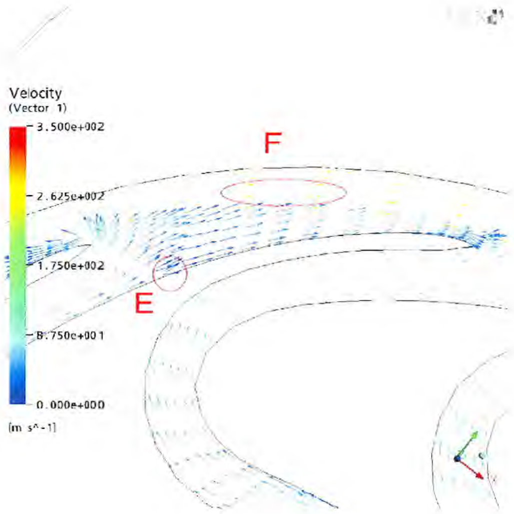

Figure 42: Mesh A - Velocity Vectors Second Passage

Figure 42, 43 and 44 show the velocity vectors for the second passage for each of the meshes, presented in the same way as before. In this passage the flow is moving faster than the first passage, and is following the direction of the blade passage as expected.

Upstream and downstream of "E" the flow is moving faster than at E. Mesh B (**Figure 43**) shows some tendency for a very small separation to form, although this is not shown in meshes A and C.

The velocity gradient across the diffuser passage is resolved in more detail as the mesh resolution increases. In Mesh C (**Figure 44**) there is a faster moving band of flow near the rotor indicated by the yellow vectors. Near the wall, and extending well into the passage there is a slower moving band of flow. The transition between these two bands is relatively abrupt in Mesh C, but this high gradient is not resolved in Mesh A (**Figure 42**). Mesh B (**Figure 43**) is intermediate between the two extremes in this respect.

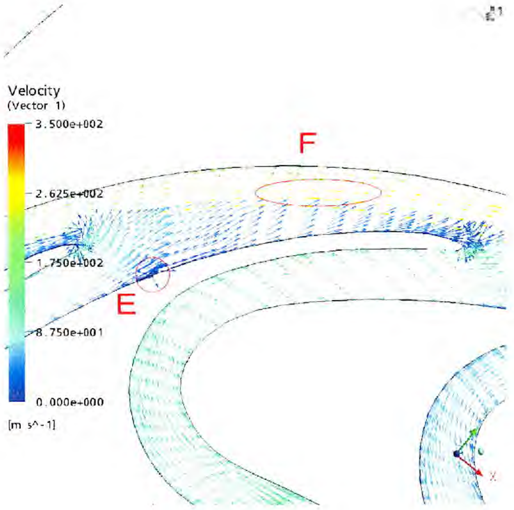

Figure 43: Mesh B - Velocity Vectors Second Passage

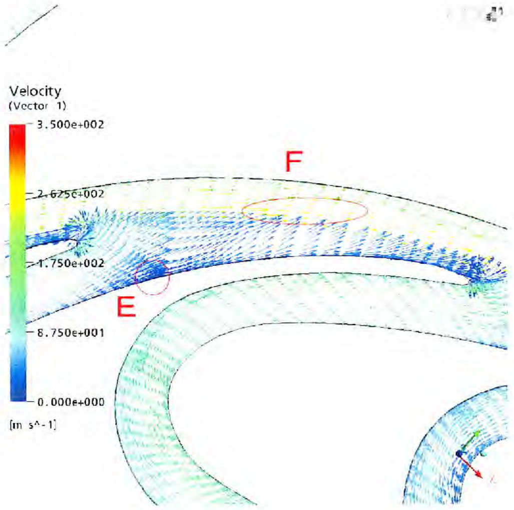

Figure 44: Mesh C - Velocity Vectors Second Passage

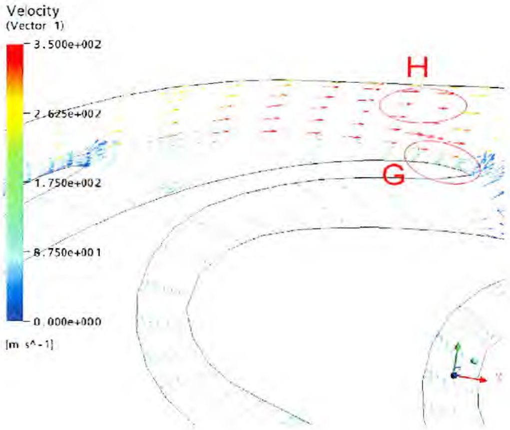

Figure 45: Mesh A - Velocity Vectors Third Passage

Figure 45, 46 and 47 show the velocity vectors for the third passage for each of the meshes, presented in the same way as before. The flow in the third passage is faster than the previous two and, in general, follows the blade passage direction.

At "G" in Mesh B (**Figure 46**) and Mesh C (**Figure 47**) there is a complex flow structure a the trailing edge of the blade. This flow structure is not shown in Mesh A (**Figure 45**). It is similar in Mesh B and Mesh C, although the mesh resolution is probably insufficient in this region.

At "H" in Mesh C (**Figure 47**), there is a band of slower moving fluid near the wall, indicated by the green arrows, and a band of fast moving fluid indicated by the red arrows near the rotor. In Mesh C the transition is relatively abrupt, but in Mesh A (**Figure 45**) the fast moving flow is seen at the diffuser wall indicated by the orange arrows. Mesh B (**Figure 46**) shows green arrows at the wall, but does not show a green band of flow as Mesh C does.

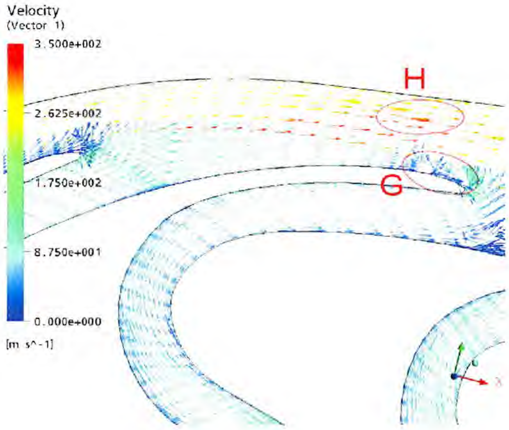

Figure 46: Mesh B - Velocity Vectors Third Passage

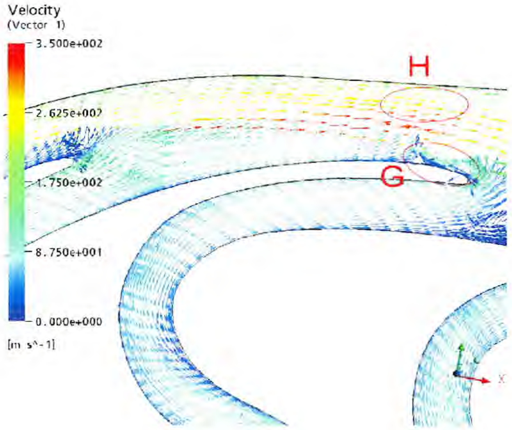

Figure 47: Mesh C - Velocity Vectors Third Passage

The results show that the solution is still changing as the mesh resolution increases, and is therefore not mesh independent. In particular the region at the trailing edge of the blade has complex flow structures and the mesh density should be increased in this region to resolve these structures.

The flow in the first passage on the suction side of the blade is in the opposite direction to the other two passages for all three meshes. Even though the solution is not mesh independent, this is evidence that a transient simulation may eventually be required to model the flow correctly.

4.9 Conclusions

This design is difficult to simulate for several reasons. Firstly the passages are long and thin, and the boundary layers are very thin. High mesh resolution perpendicular to the wall is required, and therefore mesh resolution parallel to the wall must be sacrificed to avoid a very high element count. This results in high aspect ratio elements. In addition, the flow structures in the compressor are complex and require a fine mesh in order to be resolved.

The solutions were not mesh independent. Greater computing resources are required in order to improve the mesh quality by creating finer meshes. In the light of a lack of mesh independent solutions the use of higher order differencing schemes should be considered for the convection term in the conservation equations.

The model of the exit region of the compressor should be improved in future. This is possible with new versions of CFX.

Examination of the results suggests that a transient simulation may be required, as the flow differed significantly between the passages.

5 Discussion

5.1 Comparison of Low Specific Speed Compressors

The highly forward swept compressor compares favorably with other low specific speed compressors as shown in **Table 13**. If the highly forward swept compressor were included in a multiple stage radial compressor then the Wedge and Casey compressors would be competitors. This is not a completely fair comparison, since the efficiency of the the Casey and Wedge compressors was probably measured in tests with a high inlet pressure, which would increase the Reynolds number. **Table 13** has been compiled assuming atmospheric inlet conditions. Both the Wedge and Casey compressor show high windage, although this may be a lower fraction of the total work at higher Reynolds numbers.

Table 13: Comparison of Low Specific Speed Turbocompressors

	Casey [11]	Wedge [16]	Barske [18]	Regenerative [20]	Vine
Specific Speed	0.2484	0.4108	0.0725	0.1000	0.195
Flow Coefficient	0.0040	0.0048	0.0015	0.0443	0.00675
Alternative Specific Speed	0.1842	0.2900	0.1560	0.0696	0.1357
Rotor Diameter (m)	0.2500	0.3340	0.2635	0.2820	0.21
Estimated Windage %	9.9%	13.7%	-	0.1%	2.9%
Isentropic Efficiency	50.0%	56.0%	34.5%	-	49%
Pressure Ratio	1.20	1.37	2.31	1.50	1.52
Polytropic Efficiency	51.3%	57.9%	39.8%	-	53%
Tip Speed(ms^{-1})	200	347	483	74	220
Volume Flow(m^3s^{-1})	0.0500	0.1878	0.0512	0.2600	0.065

The pressure ratio is substantially higher in the highly forward swept compressor. A single forward swept stage could replace two of Casey's stages which would have a significant impact on rotor dynamics. The polytropic efficiency is slightly higher in the highly forward swept compressor. The Wedge compressor would seem to compare more favourably with the highly forward swept compressor. However the Wedge compressor is more than double the specific speed, so the slightly better performance is not surprising. The pressure ratio is still lower than the highly forward swept compressor.

It would take two stages with a pressure ratio of 1.52 to reach the same pressure ratio as the Barske compressor. The polytropic efficiency of the highly forward swept stage is substantially greater. However the Barske compressor reaches a high pressure ratio in a single stage and is therefore simpler and cheaper.

It is difficult to make a comparison with the regenerative compressor since the specific speed is much lower, and the isentropic efficiency is not given. The specific speed of the regenerative compressor is so low that is relatively large for its flow rate. The subject of designing the highly forward swept compressor for minimum size is discussed in section 5.5.

5.2 Inter-cooling

In order to make a comparison with other compressors it is necessary to measure the efficiency. The isentropic, adiabatic efficiency is the normal efficiency used and so this convention has been adopted to allow comparisons. However cooling would reduce the work input for a given exit pressure. Low specific speed turbo-compressors offer the opportunity to inter-cool more effectively than conventional turbo-compressors, due to their large surface areas, as demonstrated by Sixsmith and Altmann[20] in the investigation of the regenerative compressor. In order to measure the isothermal efficiency of the inter-cooled compressor, it would be necessary to measure torque, or to determine the heat loss accurately.

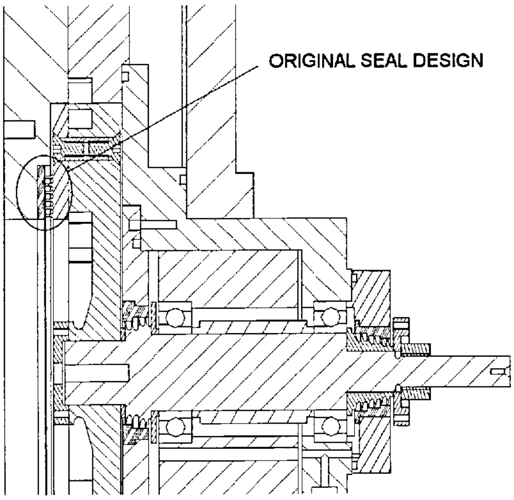

Figure 48: Original Seal Design

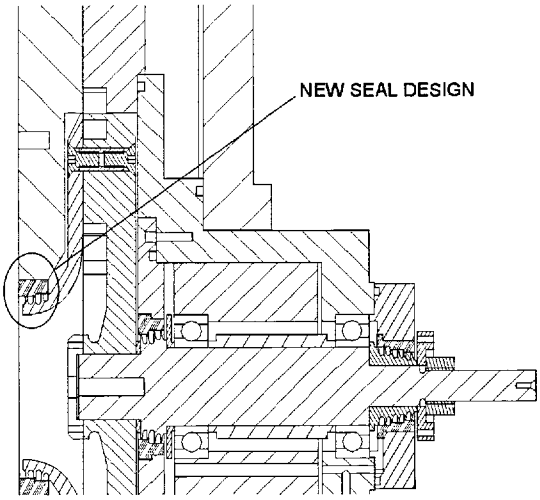

Figure 49: Proposed Seal Design

5.3 Shroud Seal Leakage

It was established in section 1.6.1 that parasitic losses were important in low specific speed machines, and that leakage was important. In the original 1D design, the static pressure at the rotor exit was similar to the inlet pressure and therefore little attention was paid to the shroud seal.

The sealing at the rotor shroud could be improved to reduce the leakage. The rotor seal is the optimum design. This design was chosen as it had been used in multistage designs because it is an axial short design. The seal has a large diameter leading to a large flow area. Since the flow rate is so low the shroud could extend to a much lower diameter and still maintain a low inlet gas speed. This would allow the leakage flow area to be reduced. Radial flow seals are not common. The main restriction to the flow is the minimum area. It is also possible to reduce the radius of the inlet to the rotor shroud since inlet velocities are low. This would allow for a much smaller leakage area. A possible layout is shown in **Figure 49** as compared to the original seal design shown in **Figure 48**.

5.4 CFD

The CFD simulation is not satisfactory due to the failure of the simulation to conserve mass.

CFX have recently produced a new version of their software which includes enhanced meshing features. All the meshes discussed so far are based on hexahedral cells. CFX 5 includes the facility to mesh and analyse geometries using tetrahedral elements. This allows the analysis of volutes and other components. Including the volute in the analysis, as discussed in Section 4.8.2, may improve the computational stability.

It will also be useful to analyse the leakage path over the shroud. The flow leaking from between the rotor and stator may affect the overall flow pattern, and the fact that there is more flow passing through the rotor than the diffuser may also have an effect. This will also be possible in future in CFX 5.

The first priority for future CFD work would be to obtain a mesh independent solution for the frozen rotor interface. It is likely that greater computer resources will be required, especially if a transient analysis is eventually required. A mesh independent solution will contribute useful information about blockage and loss factors.

5.5 Compact Design Without Manufacturing Restrictions

One of the major advantages of turbomachinery over positive displacement machines is their smaller size. This advantage has been compromised to some extent by using low specific speed compressors which are larger for a given flow rate. The mass flow rate for the low speed rig is similar to an automotive turbocharger, but the rotor is 210mm in diameter and stator is currently 370mm in diameter. The prototype design could be used in a industrial multistage radial compressor, but for a mobile application or size limited application more attention would be paid to reducing its size

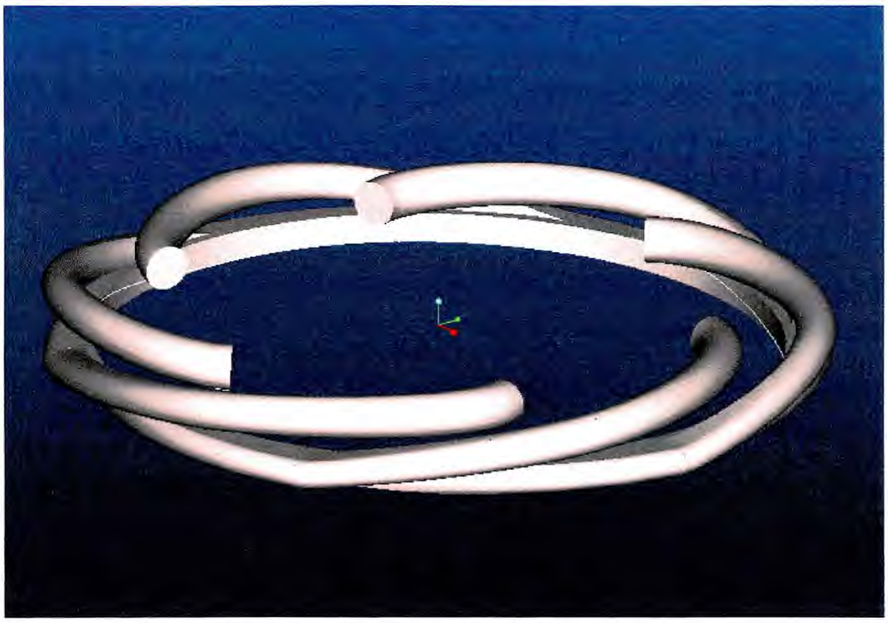

Figure 50: Concept design of a compact pipe diffuser

It is possible that a smaller overall size could be achieved by using a more flexible manufacturing method. If the diffuser ducts were more curved then the overall size of the compressor could be little bigger than the rotor itself (**Figure 50**). This design is three dimentional and therefore pipe diffusers can be used without incurring extra manufacturing cost. Pipe diffusers minimise wetted area, and prevent separated flow establishing at the corners of the diffuser ducts.

6 Conclusions

The need for low specific speed compressors has been established. They are required for the final stages in multistage radial compressors for rotor dynamic reasons. They are also needed where shaft speed is limited by cost or fixed by the constraints of other machinery. They are also required when the flow rate is so low that the shaft speeds required by normal specific speed turbo-machinery are technically unfeasible. Current low specific speed turbo-machinery designs are limited to low efficiencies and pressure ratios (typically 1.2 and 50% for conventional designs). Positive displacement machines are widely used despite their lower efficiency when compared to normal turbo-machines due to difficulties in driving a shaft at high speed.

A new concept has been established for the design of low specific compressors as a result of the need to reduce the windage on the compressor rotor, and increase the hydraulic diameter of the rotor passages. The new concept involves highly forward swept blades, and although compressors with forward swept blades can suffer from a narrow range it is possible that at low specific speed it can be stable, although it is unlikely that the new design will reach the efficiency of conventional compressors.

The concept has been demonstrated by experimental evaluation. The best performance was achieved by a machine of 20,000rpm compressing 77g/s of air drawn from the atmosphere, working at a pressure ratio of 1.52 and an efficiency of 49%.

Designs based on this concept could provide a benefit if used in the later stages of a multistage industrial compressor as the compressor that was tested has a similar specific speed and efficiency to existing designs, and a substantially greater pressure ratio.

It is likely that the performance of the compressor in this application would be superior to that measured in the laboratory tests as the final stages of a multiple stage radial compressor have a higher inlet pressure and therefore a higher Reynolds number. The design is un-optimised and therefore there is scope for improvement in the performance.

References

[1] Beith, R. Burdon, I.P. Knowles, M. *"Mirco Energy Systems"* Professional Engineering Publishing 2004 ISBN 1-86058-426-8

[2] Japikse D. and Baines N.C. *"Introduction to Turbomachinery"* Oxford University Press 1997 ISBN 0-933283-06-7

[3] Shepard, D.G. *"Principles of Turbomachinery"* Macmillan 1965

[4] Schleer, M., Mokulys, T., Abhari, R.S. *"Design of a High Pressure-ratio Centrifugal Compressor for studying Reynolds Number Effects"* Trans IMechE Compressors and Their Systems September 2001 ISBN 1 86058 417 9

[5] Casey, M.V. *"The effects of Reynolds Number on the Efficiency of Centrifugal Compressor Stages"* Journal of Engineering for Gas Turbines and Power APRIL 1985 Vol 107 541-548

[6] Cumpsty, N.A. *"Compressor Aerodynamics"* Longman 1989 ISBN 0-582-01364-X

[7] Whitfield, A. and Baines, N.C. *"Design of Radial Turbomachines"* Longman Scientific and Technical 1990. ISBN 0-582-49501-6

[8] Henneberger, S. Atlas Copco Airpower *"High-speed direct driven turbo blower"* IMechE International Conference on Compressors and Their Systems 2005 ISBN: 0-470-02576-X

[9] Vine, A.J. Thornton, W.E. Pullen, K.R. Etemad, S *"Low Specific Speed Turbocompressor"* Trans IMechE Compressors and Their Systems September 2003 ISBN 1 86058 417 9

[10] Thornton, W.E. "*Design of a Multistage Gas Compressor of Low Specific Speed*" PhD Thesis, University of London 2005

[11] Casey, M.V., Dalbert, P., Schurter, E. "*Radial Compressor Stages for Low Flow Coefficients*" IMechE paper C403/004 1990.

[12] Dalbert, P. Ribi, B. Kmeci, T. and Casey, M.V. "*Radial Compressor Design for Industrial Compressors* Journal of Mechanical Engineering Science, v 213, n 1, 1999, p 71-83

[13] Watson, N. and Janota, M. S. "*Turbocharging the internal combustion engine*" Macmillan, 1982 ISBN 0333242904

[14] Jansen, W. "*Rotating stall in a radial vaneless diffuser*" Trans. ASME Journal of Basic Engineering, (September 1964)

[15] Senoo, Y and Kinoshita, Y "*Influence of inlet flow conditions and geometries of centrifugal vaneless diffusers on critical flow angle for reverse flow*" Trans. ASME Journal of Fluids Engineering, (March 1977)

[16] Rusak, V. "*Development and Performance of the Wedge Type Low Specific Speed Compressor Wheel*" ASME 27th International Gas Turbine Conference and Exhibiton 1982

[17] Rogers, C. "*Experiments With a Low Specific Speed Partal Emmission Centrifugal Compressor*" Trans. ASME Journal of Turbomachinery January 1990 Vol 112 30-37

[18] Barske, V.M. "*Development of Some Unconventional Centrifugal Pumps*" Proc. IMechE Vol 174 (1960) 437-461

[19] Song, J. W. Raheel, M. Endgeda, A. *"A Compressible Flow Theory for Regenerative Compressors with Aerofoil Blades"* Proc. IMechE Vol. 217 Part C: Journal of Mechanical Engineering Science 2003

[20] Sixsmith, H., Altmann H. *"A Regenerative Compressor"* Trans ASME J. Engng for Industry, August 1977, 99, 637-647.

[21] Daily, J.W. and Nece, R.E. *"Chamber dimension effects on duced flow and frictional resistance of enclosed rotating disks."* Tans. ASME, J Basic Engng, 1960, 82, 217-232

[22] Romero-Hernandez, S. *"Determination of Windage Losses on High Speed Enclosed Rotating Discs with Superposed flow"* PhD Thesis, University of London 2001

[23] ABB *"2-Wire Compact Flow Meter With Digital-Signal-Processor Converter Technology"* D184S035U02 Rev. 01/01.2001

[24] Dijstentelbergen, H.H. *"The Performance of a Swirl Flowmeter"* Journal of Physics E : Scientific Instruments Vol. 3 1970

[25] Shaaban, S. Seume, J. R. *"Analysis of Turbocharger Non Adiabatic Performance"* 8th International Conference on Turbochargers and Turbocharging 2006

[26] *"CFX-TASCflow Theory Documentation Version 2.12"* AEA Technology Engineering Software Limited 2002

[27] Wilcox, D.C. *"Reassment of the Scale Determining Equation for Advanced Turbulence Models"* AIAA Vol. 26 No. 11 November 1988

[28] Launder, B.E. Sharma, B.I. *"Application of the Energy Dissipation Model of Turbulence to the Calculation of Flow Near a Spinning Disc"* Letters in Heat and Mass Transfer vol. 1, no. 2 1974, pp.131-138

[29] Bardina, J.E. Huang, P.G. Coakley, T. J. *"Turbulence Modling Validation, Testing, and Development"* NASA Technical Memorandum 110446

[30] Menter, F.R. *"Two-Equation Eddy-Viscosity Turbulence Models for Engineering Applications"* AIAA Vol. 32 No. * August 1994

[31] Massey, B.S. *"Mechanics of Fluids"* Chapman and Hall 1989 ISBN 0 412 34280 4

[32] Koumoutsos, A. Tourlidakis, A. Elder, R.L. *"Computational studies of unsteady flows in a centrifugal compressor stage"* Proceedings of the Institution of Mechanical Engineers, Part A: Journal of Power and Energy, v 214, n 6, 2000, p 611-633

[33] Moody, Lewis F. *"Friction Factors for Pipe Flow"* Trans. ASME November 1944 pp 671-684